NANO LETTERS

Letter

pubs.acs.org/NanoLett

Rapid Sequential in Situ Multiplexing with DNA Exchange Imaging in Neuronal Cells and Tissues

Yu Wang,[†,‡,§,□] Johannes B. Woehrstein,[†,‡] Noah Donoghue,[†,§,△] Mingjie Dai,[†,‡,■] Maier S. Avendaño,[†,‡] Ron C. J. Schackmann,[∥] Jason J. Zoeller,[∥] Shan Shan H. Wang,[⊥,○] Paul W. Tillberg,[▽,¶,●] Demian Park,[▽] Sylvain W. Lapan,[§] Edward S. Boyden,[#,▽] Joan S. Brugge,[∥] Pascal S. Kaeser,[⊥] George M. Church,[†,§] Sarit S. Agasti,[*,†,‡] Ralf Jungmann,[*,†,‡] and Peng Yin[*,†,‡]

[†]Wyss Institute for Biologically Inspired Engineering, [■]Program in Biophysics, Harvard University, Boston, Massachusetts 02115, United States

[‡]Department of Systems Biology, [§]Department of Genetics, [∥]Department of Cell Biology, [⊥]Department of Neurobiology, [□]Program in Biological and Biomedical Sciences, [○]Program in Neuroscience, Harvard Medical School, Boston, Massachusetts 02115, United States

[#]Department of Biological Engineering, [▽]Media Lab, [¶]Department of Brain and Cognitive Sciences, [●]Department of Electrical Engineering and Computer Science, Massachusetts Institute of Technology (MIT), Cambridge, Massachusetts 02139, United States

[△]Warren Alpert Medical School, Brown University, Providence, Rhode Island 02903, United States

Supporting Information

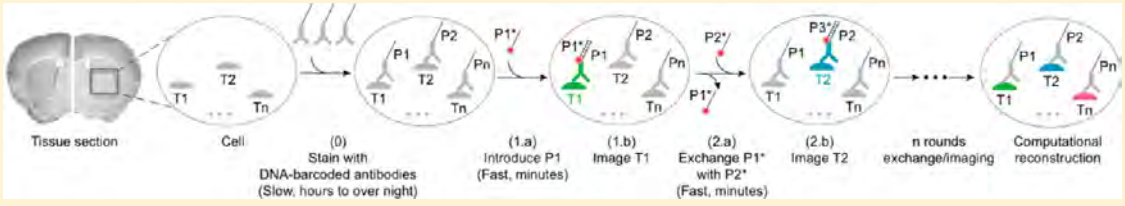

ABSTRACT: To decipher the molecular mechanisms of biological function, it is critical to map the molecular composition of individual cells or even more importantly tissue samples in the context of their biological environment in situ. Immunofluorescence (IF) provides specific labeling for molecular profiling. However, conventional IF methods have finite multiplexing capabilities due to spectral overlap of the fluorophores. Various sequential imaging methods have been developed to circumvent this spectral limit but are not widely adopted due to the common limitation of requiring multirounds of slow (typically over 2 h at room temperature to overnight at 4 °C in practice) immunostaining. We present here a practical and robust method, which we call DNA Exchange Imaging (DEI), for rapid in situ spectrally unlimited multiplexing. This technique overcomes speed restrictions by allowing for single-round immunostaining with DNA-barcoded antibodies, followed by rapid (less than 10 min) buffer exchange of fluorophore-bearing DNA imager strands. The programmability of DEI allows us to apply it to diverse microscopy platforms (with Exchange Confocal, Exchange-SIM, Exchange-STED, and Exchange-PAINT demonstrated here) at multiple desired resolution scales (from ~300 nm down to sub-20 nm). We optimized and validated the use of DEI in complex biological samples, including primary neuron cultures and tissue sections. These results collectively suggest DNA exchange as a versatile, practical platform for rapid, highly multiplexed in situ imaging, potentially enabling new applications ranging from basic science, to drug discovery, and to clinical pathology.

KEYWORDS: *Highly multiplexed imaging, super-resolution imaging, in situ protein detection, multiplexed cell type identification, in situ protein−protein colocalization analysis*

Fluorescence microscopy has become a standard tool to characterize specimens in biological and biomedical studies. One of its advantages is the widespread availability of protein-specific labeling reagents such as antibodies. However, while dye-labeled antibodies allow for easy target labeling, the spectral overlap of multiple fluorophores leads to limited multiplexing capabilities (e.g., typically no more than four targets). This shortcoming currently prevents studies targeted toward investigating network-wide changes in single cells and tissues using fluorescence microscopy. Various techniques, including "dye-cycling" by repeated antibody staining,[1−8] multiplexed ion beam imaging (MIBI),[9−11] spectrally resolved stochastic reconstruction microscopy (SR-STORM),[12] as well as others,[13−16] have been developed to overcome current limitations for multitarget detection, enabling highly multiplexed imaging studies (see Table S1 for a detailed comparison

Received: June 27, 2017
Revised: September 19, 2017
Published: September 21, 2017

DOI: 10.1021/acs.nanolett.7b02716
Nano Lett. 2017, 17, 6131−6139

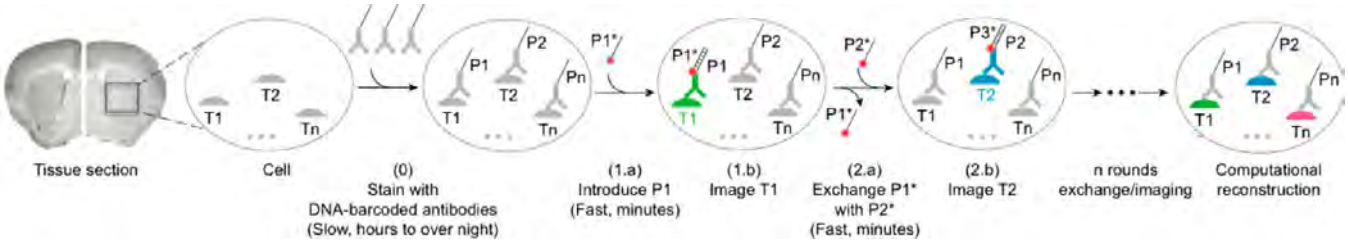

Figure 1. DNA Exchange Imaging. Distinct targets (T1, T2, ..., T*n*) are labeled using corresponding antibodies conjugated to orthogonal DNA docking strands (P1, P2, ..., P*n*) in a single step. Imager strands (P1*, P2*, ..., P*n**) are sequentially introduced to visualize target signals. The imager strands are washed away rapidly using low ionic strength buffer after each round of imaging. After imaging, all images are computationally registered, and a final merged image is reconstructed by assigning pseudocolors to each target image.

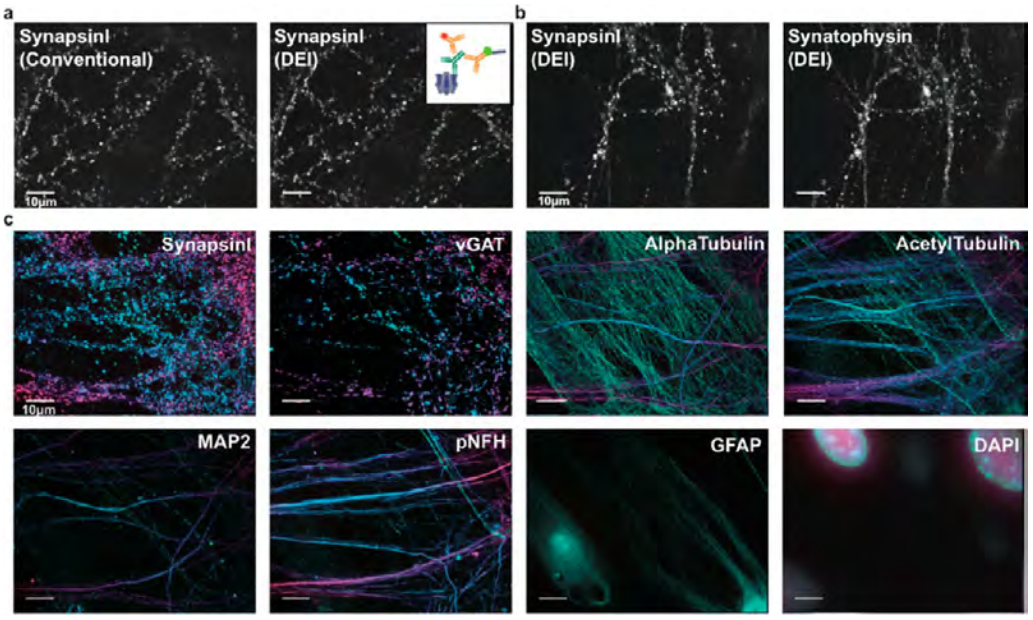

Figure 2. Multiplexed diffraction-limited confocal imaging with DEI. (a) Comparison of conventional staining using dye-conjugated antibodies and DEI using DNA-conjugated antibodies. Fixed neurons were stained with primary antibodies targeting SynapsinI, followed by both Alexa647-conjugated and DNA-conjugated antibodies, as shown in the schematic. DNA-conjugated antibody signals were visualized using Cy3b-imager strands. The correlation coefficient of the two images was 0.96. (b) Co-localization of SynapsinI and Synaptophysin in neurons visualized using two rounds of DEI. (c) Multiplexed eight-target imaging in neurons. Fixed DIV (days in vitro) 14 mouse hippocampal neurons were stained with DNA-conjugated antibodies against SynapsinI, vGAT, MAP2, pNFH, GFAP, AlphaTubulin, and AcetylTubulin. A 3D image stack of 14 μm thickness in *z*-axis was taken for each target and displayed as 2D color-coded maximum intensity projection (bottom to top: green to red). Scale bars: 10 μm. DNA docking strand sequences are listed in Table S4.

of these different techniques). However, these techniques have thus far not been broadly adopted due to practical limitations: they are typically time-intensive (e.g., due to repeated antibody staining as in current dye-cycling techniques, with each round of staining taking hours at room temperature and preferentially overnight at 4 °C for optimal labeling), and/or they are difficult to be directly implemented into current widely available microscope systems because specialized instruments are often required (e.g., as MIBI and SR-STORM).

To overcome current limitations, we introduce DNA Exchange Imaging (DEI), a generalization of our previously developed Exchange-PAINT[17] technique, providing a fast and practical method to perform highly multiplexed fluorescence imaging using standard, commercially available microscopy platforms. We have previously demonstrated DEI in the form of Exchange-PAINT.[17] In this paper, we show that the DEI principle can be generalized to other super-resolution microscopy systems, including SIM and STED, with new DNA sequence design and imaging setting. More importantly, with an optimized design, we extend DEI to standard resolution confocal microscopes that are widely available in common biological laboratories. Unlike the fluorescence "blinking" in our previous single molecule-based Exchange-PAINT, we use pseudopermanent and dense target labeling with fluorophore-conjugated complementary imager strands, thus permitting rapid image acquisition (typically <1 s exposure time) and deeper sample penetration (tens of micrometers versus a few hundred nanometers in PAINT) while maintaining the fast imager removal capability by simple and gentle buffer exchange. This unique advantage of our new protocol enables us to perform in situ multiplexing in more complex biological systems such as primary neuron cultures and biological tissue samples (as compared to thin layer of cells in our previous[17] and recent[18] super-resolution Exchange-PAINT work).

In DEI, we employ DNA-barcoded antibodies—instead of dye-labeled antibodies—that are conjugated with short DNA oligos (typically 9–10 nucleotides long for implementations in this paper) called docking strands.[17−19] Multiplexed protein

DOI: 10.1021/acs.nanolett.7b02716
Nano Lett. 2017, 17, 6131−6139

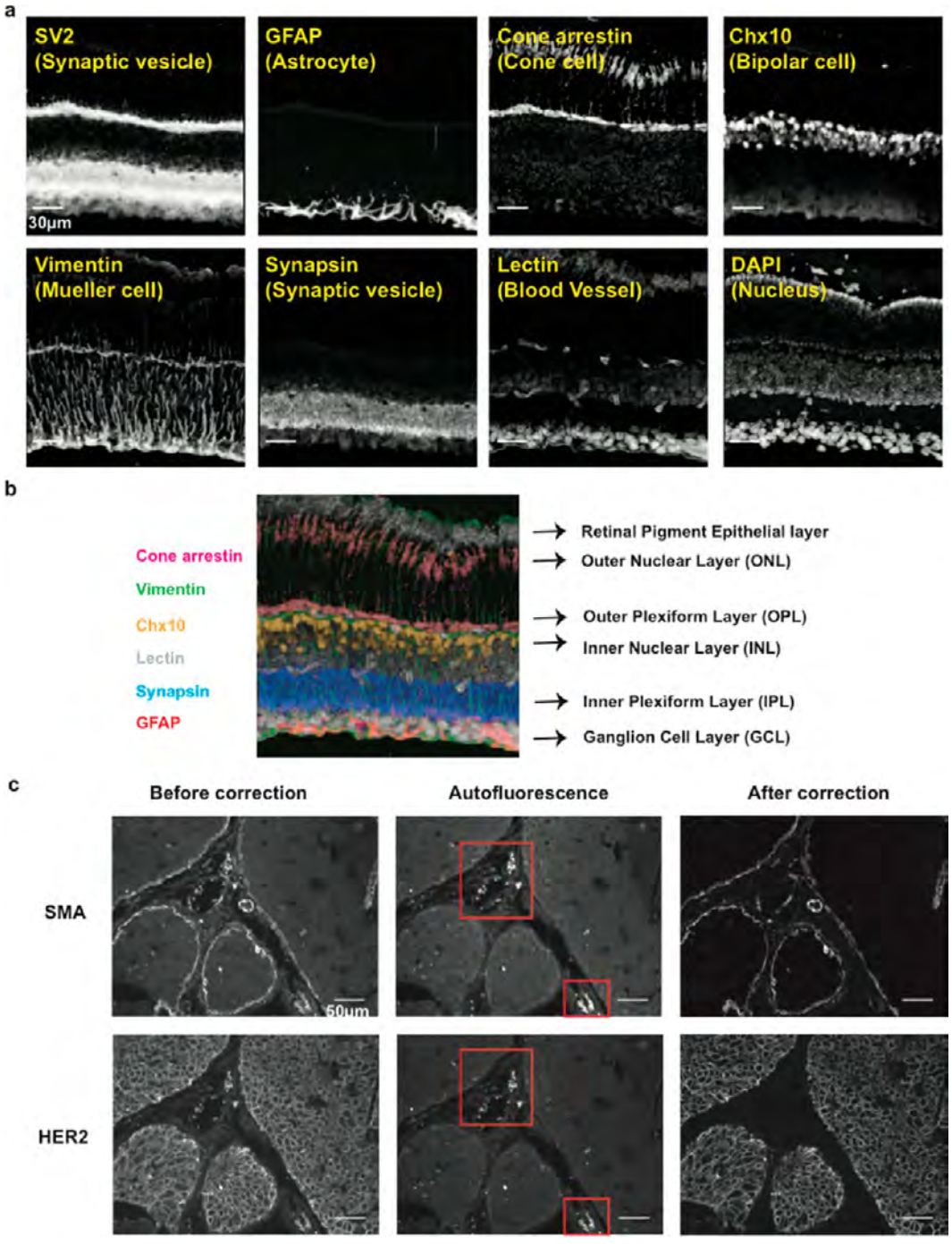

Figure 3. Multiplexed DEI of tissue samples. (a) A 40 μm thick fresh frozen mouse retina section was stained with antibodies targeting SV2, GFAP, Cone arrestin, Chx10, Vimentin, and Synapsin. 3D images were taken with six rounds of exchange of Cy3b-labeled imager strands. Blood vessels were stained with Alexa488-conjugated lectin probes and imaged in every exchange cycle for image registration. The nucleus was stained with DAPI. Scale bars: 30 μm. (b) Merged six-target image reveals different layers of cells in the retina. (c) Autofluorescence correction with DEI on a paraffin-embedded breast tumor section. Autofluorescence images were taken before adding imager strands with the same laser intensity and camera exposure time and then subtracted from the corresponding target images to obtain autofluorescence-corrected images. Note that the strong autofluorescence (presumably from blood cells, labeled with red square) was eliminated in the corrected images. Scale bars: 50 μm. DNA docking strand sequences are listed in Tables S5 and S7.

target labeling is performed efficiently by single-step simultaneous immunostaining with antibodies carrying orthogonal DNA docking strands, followed by image acquisition where dye-labeled complementary imager strands are applied sequentially via rapid buffer exchange (Figure 1). We demonstrated 8-target imaging in primary neuron cultures and in tens of micro thick retina tissue sections in 2−3 h (as compared to days required in principle by previous methods using comparable equipment) to visualize distinct cellular structures and to annotate different cell types. In addition to providing a rapid and simple multiplexed imaging method, Exchange Confocal, as well as other DEI methods, enables easy autofluorescence correction, and is naturally chromatic aberration-free and photobleaching-resistant (Figure S1).

DOI: 10.1021/acs.nanolett.7b02716
Nano Lett. 2017, 17, 6131−6139

Exchange-PAINT[17] has been previously developed to perform multiplexed single-molecule localization-based SR imaging. Despite its superior resolution, its utility is restricted due to its imaging time and depth trade-off. It requires recording a time-lapse movie of single molecule blinking events for final SR image reconstruction, which typically takes minutes to even hours for a single reconstructed image. In addition, the high signal-to-noise ratio requirement for PAINT imaging, single-molecule-compatible microscopes (usually total internal reflection fluorescence microscopes) are necessary, limiting the imaging depth to typically a few hundred nanometers above the coverslip. Moreover, diffraction-limited imaging is often sufficient for experiments that only require single-cell resolution (e.g., pathological analysis). In SR PAINT imaging, sparse labeling of targets with transiently binding imager strands is required for single-molecule localization. In contrast, diffraction-limited Exchange-Confocal imaging shown here aims to capture signals from all of the molecules of a certain target in a single image frame, which requires pseudopermanent and dense target labeling with imager strands. To achieve this, we tuned three parameters: imager/docking strand association time, imager strand concentration, and camera exposure time. First, we designed imager/docking strand duplexes with higher binding affinity to attain a relatively slow dissociation rate (0.2 s^{-1} for a 10 base-pair duplex on average[19]) by increasing the length of the DNA duplex (Figure S2). To minimize the number of unoccupied docking sites, we used a high concentration of imager strand (e.g., 10 nM as compared to 1 nM in single-molecule PAINT applications) to densely label the docking sites for the corresponding target (Figure S2). Furthermore, we used longer camera exposure times (typically 50−300 ms for a widefield microscope and 500 ms to 5 s for a spinning disk confocal microscope) to minimize unoccupied docking sites and enhance the signal-to-noise ratio.

As a result, we achieved diffraction-limited Exchange-Confocal imaging with a quality comparable to that of conventional IF methods. To examine signal specificity of Exchange-Confocal, we compared the Exchange-Confocal images with those attained by conventional IF methods using fluorophore-conjugated antibodies (Figure 2a and Figure S3). We labeled synapses with the marker protein SynapsinI using primary antibodies followed by secondary antibodies conjugated either with DNA docking strands or with Alexa488 dye. The SynapsinI signals from Exchange-Confocal and from conventional IF were obtained with 561 nm and with 488 nm excitation, respectively. We observed colocalization of fluorescence signals from these two methods with a correlation coefficient of 0.96. We also performed Exchange-Confocal based colocalization analysis of SynapsinI and Synaptophysin, both of which are present in synaptic vesicles (Figure 2b). We obtained a correlation coefficient of 0.80, which is similar to values that have been reported using array tomography.[20]

As Exchange-Confocal requires sequential application of imager strands labeled with the same fluorophore, the efficient imager strand removal is critical. We tested changes in fluorescence intensity between each cycle of imager strand exchange (Figure S4). DIV14 mouse hippocampal neurons were fixed and stained with antibodies against glial fibrillary acidic protein (GFAP, a marker protein for astrocytes) and beta3Tubulin (a marker protein for neurons). P1* and P2* imager strands were sequentially applied to visualize GFAP and beta3Tubulin, respectively. The fluorescence intensity after washing with PBS decreased to the background level and thus was negligible compared to signal levels in the other images, confirming the sufficiently efficient removal of imager strands from the solution.

To demonstrate multiplexed Exchange-Confocal, we next imaged eight targets in a fixed primary mouse hippocampal neuron culture (Figure 2c and Movie 1). SynapsinI antibodies were used to mark all synapses, and vesicular GABA transporter (vGAT) antibodies labeled inhibitory synapses. Five other structural proteins were also labeled, including microtubule associated protein 2 (MAP2) (a dendritic marker), phosphorylated neurofilament heavy chain (pNFH) (in neurites), AlphaTubulin (microtubule component), AcetylTubulin (microtubule component), and GFAP (an astrocyte marker). DAPI was used to stain nuclei. For the eight protein targets, we performed dual-color imaging (using Cy3b- and Atto655-conjugated imager strands) to reduce probe exchange cycles. The sample drift was monitored by signals from the 488 nm channel, and images were registered accordingly (Figure S5).

Three-dimensional (3D) images were taken for each target using a spinning disk confocal microscope, and the color-coded 2D maximum projection images were displayed for each target (Figure 2c). We used green and red colors to represent the signals from the bottom and top focal planes, respectively. A color gradient from green to red was used to represent the signals from intermediate focal planes. Astrocytes, labeled with GFAP, were mostly shown in green, consistent with the fact that astrocytes grew beneath neurons. SynapsinI labeled both excitatory and inhibitory synapses, while vGAT only labeled inhibitory synapses. As expected, SynapsinI signals were more abundant than those of vGAT. AlphaTubulin was observed in both astrocytes and neurons across the whole z-stack, and acetylTubulin was highly expressed in neurons.

To test the applicability of Exchange-Confocal to tissue samples, we performed eight-target Exchange-Confocal in fresh-frozen mouse retina tissue sections (Figure 3a and b). We chose retina samples because the tissue organization has been intensively studied and different cell types can be distinguished using protein markers.[21,22] A 40 μm thick retina section was stained using DNA-conjugated antibodies against SV2, GFAP, Cone arrestin, Chx10, Vimentin, and Synapsin and imaged with six rounds of exchange using Cy3b-conjugated imager strands. Lectin-Alexa488 was used to stain blood vessels and imaged for every exchange cycle for image registration. DAPI was used to stain the nucleus. As expected, every protein species was truthfully detected using Exchange-Confocal with the distribution of each target being in line with previous reports.[21−23] SV2 and Synapsin are both located in synapses. SV2 exists in both outer plexiform layer (OPL) and inner plexiform layer (IPL), whereas Synapsin is only located in the IPL, similar to what has been reported in salamander retina[24] (Figure 3b). It should be noted that SynapsinI antibody was used to stain the sample and the lack of Synapsin signal in the OPL only reflects the absence of SynapsionI, which could be replaced by alternative forms of Synapsin, such as Synapsin II or III. GFAP marks astrocytes that are located close to the ganglion cell layer (GCL) and Muller glial endfeet. Cone arrestin marks the cone photoreceptor cells in the outer nuclear layer (ONL). Vimentin labels Muller cells that spread across multiple layers. Chx10 is a pan-bipolar cell marker[23] located in the inner nuclear layer (INL). Another five-target Exchange-Confocal experiment was performed on a 10 μm thick formaldehyde fixed mouse brain section (Figure S6).

DOI: 10.1021/acs.nanolett.7b02716
Nano Lett. 2017, 17, 6131−6139

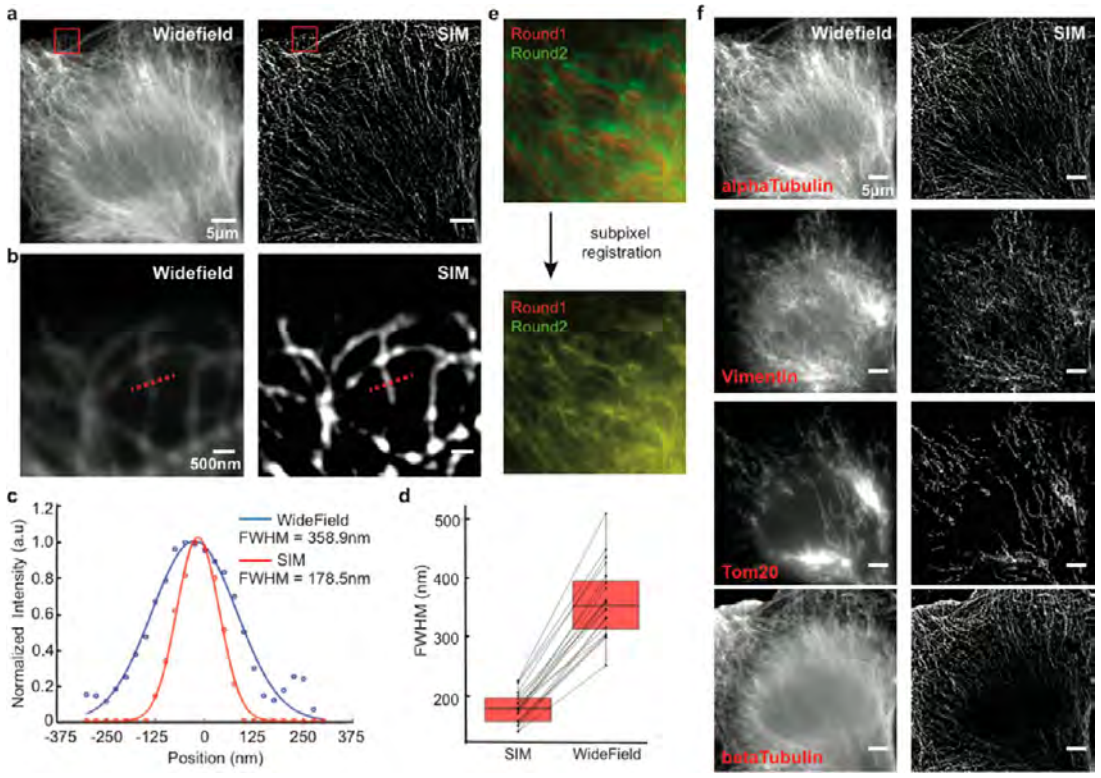

Figure 4. Four-target DEI with SIM in BSC1 cells. (a) Comparison of wide-field and SIM images on alphaTubulin. Scale bars: 5 μm. (b) Zoom-in views of the microtubules highlighted by red square in panel a. (c) Measurement of the apparent width of microtubules using a full-width at half-maximum (fwhm) criterion. The intensity plot of the cross-section highlighted in panel b was fitted using a Gaussian. (d) fwhm measurement of 20 microtubule cross sections revealed 2.014 ± 0.045 fold reduction of fwhm (the error range is SEM; boxes denote median values ± quartiles). (e) Subpixel registration of images in different exchange rounds. Vimentin was stained with both DNA-conjugated and Alexa488-labeled antibodies, and the 488 nm channel used for image registration. (f) Multiplexed 3D Exchange-SIM imaging in BSC1 cells. The 2D maximum intensity projections are presented here. Scale bars: 5 μm. DNA docking strand sequences are listed in Table S8.

We also tested Exchange-Confocal in paraffin-embedded tissue samples and performed two rounds of probe exchange to visualize HER2 and smooth muscle actin (SMA) in a 4 μm formalin-fixed and paraffin-embedded intraductal breast tumor carcinoma tissue from a HER2+ xenograft of SUM225 tumor cells[25] (Figure 3c). SMA stains the myoepithelial cells surrounding the intraductal tumor as well as stromal fibroblasts. We also note that Exchange-Confocal permits simple autofluorescence correction, an additional advantage over conventional fluorescence imaging for tissue samples. Autofluorescence, caused by the presence of various endogenous molecules (e.g., reduced NAD(P)H, flavins, reticulin fibers, lipofuscins, elastin, and collagen), can mask true target signals.[26] Although a few approaches have been developed, such as autofluorescence quenching using Sudan Black B, photobleaching with high intensity lasers, and postmeasurement image correction using complex mathematical models, they require optimization specific for each type of sample and/or may cause sample damage if harsh treatment is performed.[26] When performing DEI—as fluorophore-tagged imager strands are not added until the sample is ready to be imaged on the microscope—an image exhibiting only autofluorescence can be acquired immediately before the addition of imager strands and subsequently subtracted from the true target image. In Figure 3c, autofluorescence signals were captured before the addition of imager strands in the same field of view. Compared with images before correction, the "false" signals indicated by the red arrows were significantly reduced in the corrected images. It should be noted that the laser intensity and camera exposure time for autofluorescence images should be identical to those used for the real target image to ensure accurate correction.

Although diffraction-limited Exchange-Confocal enables faster and deeper sample imaging, its resolution may not be sufficient to address certain biological questions that require subcellular resolution. To achieve this, we applied DNA-Exchange-Imaging to various fast SR imaging microscopy platforms. First, we performed DEI using structured illumination microscopy (SIM), which doubles the achievable resolution.[27] Here in Exchange-SIM, we stained BSC1 cells with antibodies against AlphaTubulin followed by DNA-conjugated secondary antibodies (Figure 4a and b). We measured the full width at half-maximum (fwhm) of microtubules by Gaussian fitting the intensity plot of 20 microtubule cross sections and obtained an average of ~2-fold reduction of fwhm, consistent with the theoretical resolution enhancement for commercial SIM microscopes (Figure 4c and d and Table S11). While improving spatial resolution helps to resolve fine molecular structures, it also renders the experiment more sensitive to sample drift during buffer exchange process. To reduce drift-induced errors, we adapted a phase correlation-based algorithm[28] to perform subpixel registration (see Methods for more details). The algorithm correctly identified sample drift between different exchange cycles and registered images accordingly (Figure 4e). Multiplexed SIM imaging was performed with four rounds of exchange with Cy3b-conjugated imager strands targeting alphaTubulin, Vimentin, Tom20, and

DOI: 10.1021/acs.nanolett.7b02716
Nano Lett. 2017, 17, 6131−6139

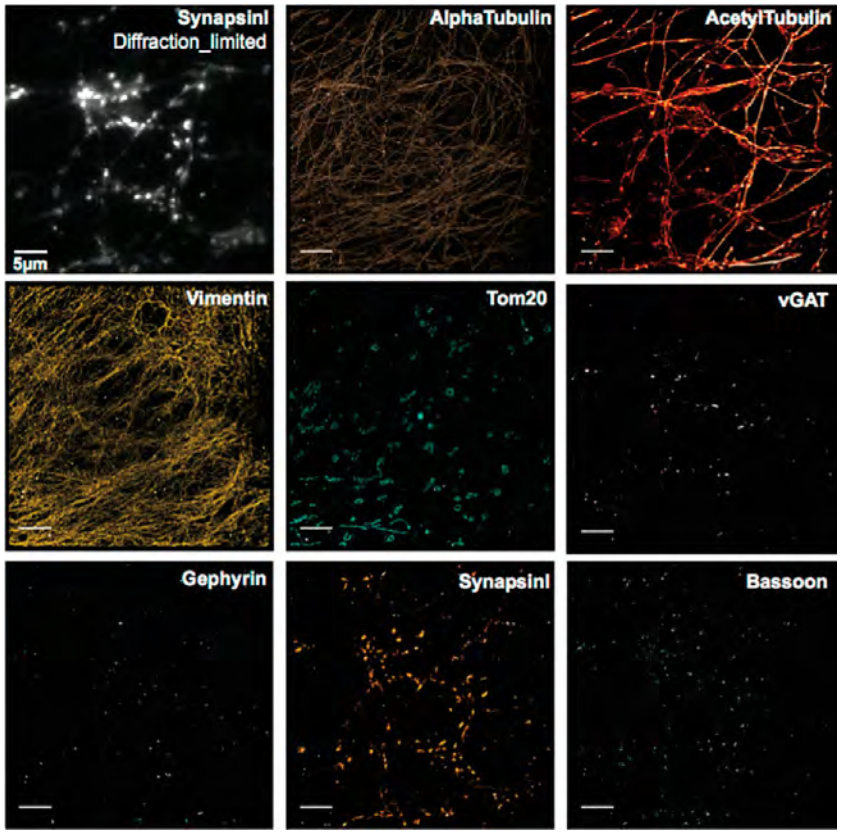

Figure 5. Eight-target chromatic aberration-free Exchange-PAINT imaging in primary neurons. Fixed DIV14 mouse hippocampal neurons were stained with DNA-conjugated antibodies targeting AlphaTubulin, Vimentin, vGAT, Gephyrin, SynapsinI, Bassoon, AcetylTubulin, and Tom20. SynapsinI was additionally labeled with Alex488-conjugated secondary antibodies for selecting regions of interest. In total, eight rounds of Exchange-PAINT imaging with Atto655-conjugated imager strands were performed to visualize all targets. Scale bar: 5 μm. DNA docking strand sequences are listed in Table S10.

betaTubulin (Figure 4f). An upsampling factor of 5 in the *x*- and *y*-axes and a factor of 2 in *z*-axis were used to perform subpixel image registration, resulting in a subpixel precision of 5 nm in the *x* and *y*-axes and 75 nm in the *z*-axis.

A similar multiplexed experiment was performed using a STED microscope (Figure S7). Together with previous related Exchange-STED work applied to synthetic DNA nanostructures,[29] our results show that DEI is generally compatible with SIM and STED microscopy and can be used for rapid multiplexed SR imaging.

For even higher spatial resolutions, we turned to our previous Exchange-PAINT[17] method and demonstrated eight-target super-resolution imaging in cultured neurons. DIV14 mouse hippocampal neurons were fixed and stained with antibodies against AcetylTubulin, AlphaTubulin, Vimentin, Tom20, SynapsinI, Bassoon, vGAT, and Gephyrin, utilizing our recently developed DNA-antibody labeling chemistry.[18] While synapsinI and vGAT antibodies label all and inhibitory synaptic vesicle clusters, respectively, Bassoon is a marker for the presynaptic active zone, and gephyrin marks postsynaptic scaffolds at inhibitory synapses. AcetylTubulin and AlphaTubulin are both microtubule components. Vimentin is a protein component in intermediate filaments, and Tom20 is located in the mitochondria. Eight rounds of Exchange-PAINT imaging with Atto655-conjugated imager strands were performed to visualize each target (Figure 5).

To demonstrate the improvement in resolution, we compared the quality of diffraction-limited and SR images for microtubules and merged Bassoon and Gephyrin from Figure 5 (Figures S8 and S9). Individual microtubule filaments were clearly resolved in the SR image but not in the diffraction-limited image (Figure S8a and b). A region was selected for a magnified view with two microtubules in close proximity to each other, and the distance between the two filaments was measured to be 108 nm (Figure S8c and d). In the Bassoon and Gephyrin merged image, presynaptic Bassoon signals can be distinguished from the postsynaptic Gephyrin signals in the SR image but not in the diffraction-limited image (Figure S9).

One unique application of multiplexed imaging is to detect protein−protein colocalization. To test the applicability of Exchange-PAINT for such studies, we merged the four synaptic protein images from Figure 5 to assay colocalization of these proteins (Figure 6a). We first compared the diffraction-limited and super-resolution images. Individual synapses are difficult to distinguish from each other in the diffraction-limited images but can be clearly visualized in the super-resolution images (Figure 6b). Particularly, the synapse orientation can be detected by lining synapsin (synaptic vesicle marker that is further from the presynaptic membrane), Bassoon (active zone marker that is closer to the presynaptic membrane) and gephryin (postsynaptic density marker on the postsynaptic sites) (Figure 6b). We also selected one region for a magnified view (Figure 6c). SynapsinI and Bassoon are known to be present in both excitatory synapses and inhibitory synapses, whereas vGAT and Gephyrin selectively label inhibitory synapses.[20] Three synapses were included in this region. Two of them contained only

DOI: 10.1021/acs.nanolett.7b02716
Nano Lett. 2017, 17, 6131−6139

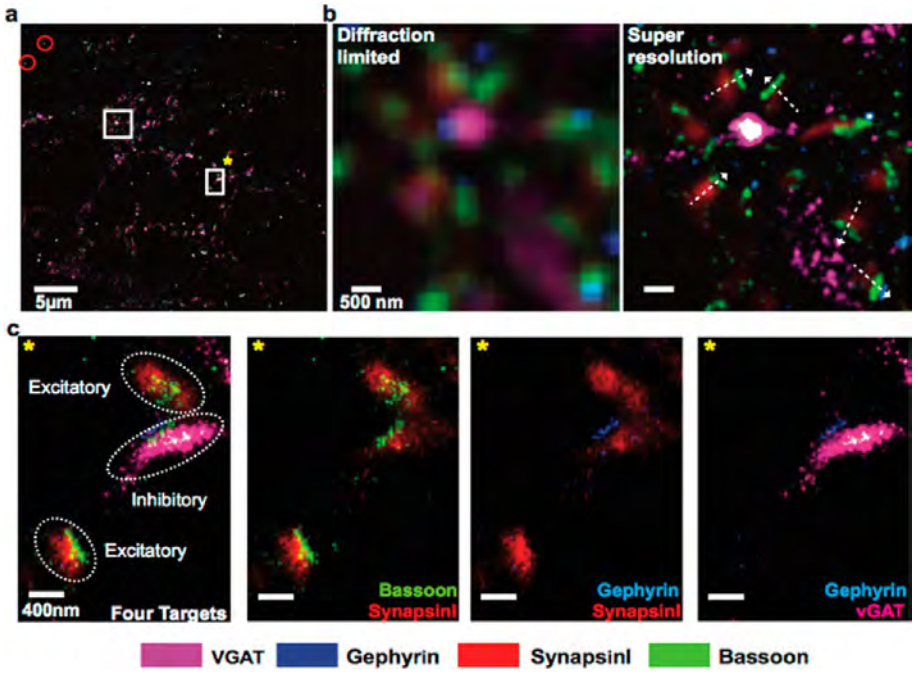

Figure 6. Co-localization of synaptic proteins detected using multiplexed Exchange-PAINT imaging. (a) The images of synaptic proteins from Figure 5 were merged using gold nanoparticles as registration markers (highlighted with red circles). Scale bar: 5 μm. (b) Comparison of diffraction-limited and super-resolution images of four synaptic proteins from the region highlighted with a white square without *. The orientation of synapses could be visualized in the super-resolved image as indicated by the white dashed arrows. Scale bar: 500 nm. (c) One region from panel a was selected for a magnified view (highlighted with a white square with *). Scale bars: 400 nm.

SynapsinI and Bassoon signals, suggesting they were excitatory synapses, whereas the middle synapse contained all four targets, indicating that it was an inhibitory synapse (Figure 6c). SynapsinI, Bassoon, and vGAT were present in the presynaptic site and therefore well-separated from the signal from Gephyrin that existed in the postsynaptic site. The distribution patterns of SynapsinI and vGAT, both of which were localized on synaptic vesicles, correlated well with each other. The result indicates Exchange-PAINT is well-suited for high-resolution visualization of protein−protein colocalization in situ.

An increasing body of effort has been devoted to molecular heterogeneity mapping in single cells. Such in situ "omics" studies, including transcriptomics and proteomics, have the potential to greatly expand our knowledge about how cells and tissues are organized to realize their biological functions. Several techniques, such as laser capture microdissection-assisted single-cell RNA sequencing,[30] Fluorescence in situ RNA sequencing,[31] highly multiplexed FISH,[32] has been developed to enable spatially resolved transcriptomics. In situ proteomics analysis, on the other hand, has not been widely performed mainly due to the lack of efficient and practical methods, particularly as existing sequential IF imaging methods require multirounds of time-intensive immunostaining. DEI herein provides a simple, efficient, and versatile tool to map diverse proteins in situ with flexible choice regarding achievable spatial resolution. It has multiple advantages: (1) DEI allows fast multiplexed data acquisition and probe exchange, as targets are simultaneously immunostained and transient binding of imagers to docking strands is rapid (minutes); (2) DEI—as other sequential imaging approaches−allows image acquisition with a single laser line, thus avoiding chromatic aberration (Figure S10) and eliminating time-consuming optimization of imaging setting (e.g., immersion medium for SIM) for individual laser channels; (3) DEI allows straightforward reimaging of earlier targets. This allows users to rapidly scan a sample e.g. using fast Exchange-Confocal to determine regions of interest and then reprobe these with shorter imager strands for higher resolution imaging, for example, using Exchange-PAINT; (4) DEI does not require specialized instruments (e.g., mass spectrometers for MIBI) or harsh buffer treatment (e.g., acidified $KMnO_4$ or H_2O_2) to quench fluorescence signals. The labeling protocols and imaging instruments are identical to standard and well-established immunostaining methods, the only difference being the use of a DNA-tagged antibody as opposed to a dye-tagged antibody, thus making it easily accessible to common biological laboratories.

A key requirement for sequential imaging is to minimize sample drift during an experiment. All of our buffer exchange experiments were performed without removing samples from the microscope stage. A fluidic chamber system has been described in our original Exchange-PAINT paper[17] and can be used to reduce the physical disturbance caused by buffer exchange. A registration marker channel, either bright field or other fluorescence channels, is required to record sample drift for postexperiment image registration. In this current study, we adapted a subpixel registration algorithm[28] that can perform translation drift correction with a user-defined up-sampling factor. It increased the registration accuracy, which is important when super-resolution imaging is performed. *Z*-axis drift can be easily managed by using commercially available focus maintaining systems.

We note that we occasionally observe nonspecific nuclear staining from DNA-conjugated primary antibodies, which is likely an antibody-specific phenomenon. Interestingly, we did not observe a similar phenomenon for DNA-conjugated secondary antibodies (Figure S11). It has been suggested that the addition of dextran sulfate to the incubation buffer can

DOI: 10.1021/acs.nanolett.7b02716
Nano Lett. 2017, 17, 6131−6139

alleviate the nonspecific binding.[33] The addition of Herring sperm DNA and polyT DNA has also been used to block nonspecific interaction caused by DNA.[14] We also notice that using saponin instead of Triton or Tween as detergent during staining does not permeabilize the nucleus membrane and hence prevents antibodies from entering the nucleus.

In summary, we have developed DNA-Exchange-Imaging as a rapid and versatile multiplexed imaging technique for both diffraction-limited and super-resolution in situ imaging in cells and in tissues. The intrinsic programmability of imager/docking strand interaction renders DEI easily adaptable to diverse imaging platforms, including standard resolution Exchange-Confocal demonstrated here, and various super-resolution methods including Exchange-SIM demonstrated here, Exchange-STED demonstrated here and in related work,[29] Exchange-STORM demonstrated in our recent related work using stably attached imager strands,[34] and Exchange-PAINT[17] demonstrated in our original work with increasing resolution. We further compared these three binding schemes (i.e., transient, semitransient, and stable binding) in Figures S2, S12, and S13, and list their pros, cons, and suitable application in Table S12. In short, the transient binding scheme enables easy DNA strand exchange but gives weak signals under the same imaging setting. In contrast, the stable binding scheme gives strong signals but requires harsher strand removal methods (i.e., formamide-containing solution). The semitransient binding retains the feature of easy DNA strand exchange and gives medium-level signals. In addition, the transient-binding scheme is suitable for DNA-PAINT super-resolution imaging. Meanwhile, the semitransient binding and stable binding schemes enable highly multiplexed confocal, SIM, STED imaging. The stable binding scheme also allows STORM imaging. Finally, the signals from both transient binding and semitransient binding schemes are tunable based on imager strand concentration and resistant to photobleaching because of replenishment of imager strands from the solution. One concern for semitransient binding compared to stable binding is that the excessive imager strands in the solution could contribute to the background and hence reduce image quality. We found that image processing (e.g., deconvolution) can be used to address the background issue and improve image quality (Figure S14). This will serve a guideline for users to choose the binding scheme based on their experiments.

Beyond these validated imaging platforms, we also expect that DEI is compatible with many other imaging methods. For example, a combination of DEI with ultrathin sectioning of samples could allow correlative light and electron microscopy imaging. Additionally, DEI is also in principle compatible with DNA mediated in situ signal amplification methods (e.g., hybridization chain reaction,[35] and rolling circle amplification[36]), potentially permitting rapid, spectrally unlimited multiplexing for low abundance targets. Combination of DEI with tissue clearing methods, such as CLARITY[37] and SWITCH,[38] would allow the imaging of a thick tissue sample. The combination of DEI with expansion microscopy[33] would further allow imaging thick samples with nanoscopic resolution. The integration of DEI with neuron tracing techniques, such as Brainbow,[39] could allow simultaneous detection of neuronal connectivity and underlying molecular characteristics, such as cell identity. The resultant "Molecular Connectome" would complement the "Anatomical Connectome"[40] and help us understand brain function across multiple scales from circuits to molecules.

■ ASSOCIATED CONTENT

Supporting Information

The Supporting Information is available free of charge on the ACS Publications website at DOI: 10.1021/acs.nanolett.7b02716.

(1) Methods (cell culture and tissue samples preparation and staining; imaging setup and acquisition; imaging analysis); (2) Supplementary Figures 1−14 (photobleaching resistance; comparison of DNA labeling schemes; exchange-STED); (3) Supplementary Tables 1−12 (comparison of DNA labeling schemes; comparison of multiplexed imaging methods; lists of DNA sequences; lists of antibodies) (PDF)

(1) 3D views of multi-targets in fixed mouse hippocampal neuron cultures. A movie was created using Imaris for 3D slicing views of the targets shown in Figure 2. Mouse hippocampal neurons were fixed using PFA and stained to target SynapsinI, vGAT, MAP2, pNFH, AlphaTubulin, AcetylTubulin, GFAP, and DAPI (AVI)

■ AUTHOR INFORMATION

Corresponding Authors

*E-mail: (P.Y.) py@hms.harvard.edu; 617-432-7731.
*E-mail: (R.J.) jungmann@biochem.mpg.de.
*E-mail: (S.S.A.) sagasti@jncasr.ac.in.

ORCID

Ralf Jungmann: 0000-0003-4607-3312
Peng Yin: 0000-0002-2769-6357

Present Addresses

S.S.A.: New Chemistry Unit and Chemistry & Physics of Materials Unit, Jawaharlal Nehru Centre for Advanced Scientific Research (JNCASR), Bangalore, India.
J.B.W., R.J.: Department of Physics and Center for Nanoscience, Ludwig Maximilian University, 80539 Munich, Germany, Max Planck Institute of Biochemistry, 802152 Martinsried near Munich, Germany.

Notes

The authors declare the following competing financial interest(s): P.Y., R.J., S.A.A., and Y.W. have filed a patent application for the reported technology. P.Y. and R.J. are cofounders of Ultivue, Inc., a startup with interests in commercializing DNA-Exchange-Imaging technology. P.Y. is also a cofounder of NuProbe Global. G.M.C. is a cofounder of ReadCoor, Inc.. E.S.B. is a cofounder of Expansion Technologies, Inc.

■ ACKNOWLEDGMENTS

We thank X. Chen, F. Schueder, and C. Cepko for helpful discussions. We thank Z. Liang for kindly providing experimental materials. We thank L. Ding from Enhanced Neuroimaging Core in Harvard for assistance in STED microscopy. This work is supported by NIH grants (1U01MH106011, 1R01EB018659), NSF grant (CCF-1317291), and ONR grants (N00014-13-1-0593 and N00014-14-1-0610) to P.Y.; Emmy Noether Fellowship (DFG JU 2957/1-1), ERC Starting Grant (MolMap, Grant agreement number 680241) and support from Max Planck Society to R.J.; Wellcome Trust-DBT India Alliance Intermediate Fellowship (IA/I/16/1/502368) to S.S.A.; NIH grant (RM1HG008525) to G.M.C.; NIH grant (R01NS083898) to P.S.K.; NIH grant (P01 CA080111.) to J.S.B.; NIH grants (1R24MH106075,

DOI: 10.1021/acs.nanolett.7b02716
Nano Lett. 2017, 17, 6131−6139

NIH 1R01NS087950, and NIH 1R01MH103910), and support from HHMI-Simons Faculty Scholars Program, the Open Philanthropy project, the MIT Media Lab, and the New York Stem Cell Foundation to E.S.B.. Y.W. acknowledges support from the Chinese Scholarship Council. M.S.A. and M.D. acknowledge support from HHMI International Student Research Fellowships. S.S.H.W. acknowledges support from NSF fellowship DGE1144152. P.W.T. acknowledges support from the Hertz Foundation.

REFERENCES

(1) Friedenberger, M.; Bode, M.; Krusche, A.; Schubert, W. *Nat. Protoc.* **2007**, *2* (9), 2285−94.
(2) Gerdes, M. J.; Sevinsky, C. J.; Sood, A.; Adak, S.; Bello, M. O.; Bordwell, A.; Can, A.; Corwin, A.; Dinn, S.; Filkins, R. J.; Hollman, D.; Kamath, V.; Kaanumalle, S.; Kenny, K.; Larsen, M.; Lazare, M.; Li, Q.; Lowes, C.; McCulloch, C. C.; McDonough, E.; Montalto, M. C.; Pang, Z.; Rittscher, J.; Santamaria-Pang, A.; Sarachan, B. D.; Seel, M. L.; Seppo, A.; Shaikh, K.; Sui, Y.; Zhang, J.; Ginty, F. *Proc. Natl. Acad. Sci. U. S. A.* **2013**, *110* (29), 11982−7.
(3) Glass, G.; Papin, J. A.; Mandell, J. W. *J. Histochem. Cytochem.* **2009**, *57* (10), 899−905.
(4) Lin, J. R.; Fallahi-Sichani, M.; Sorger, P. K. *Nat. Commun.* **2015**, *6*, 8390.
(5) Micheva, K. D.; Smith, S. J. *Neuron* **2007**, *55* (1), 25−36.
(6) Pirici, D.; Mogoanta, L.; Kumar-Singh, S.; Pirici, I.; Margaritescu, C.; Simionescu, C.; Stanescu, R. *J. Histochem. Cytochem.* **2009**, *57* (6), 567−75.
(7) Schubert, W.; Bonnekoh, B.; Pommer, A. J.; Philipsen, L.; Bockelmann, R.; Malykh, Y.; Gollnick, H.; Friedenberger, M.; Bode, M.; Dress, A. W. *Nat. Biotechnol.* **2006**, *24* (10), 1270−8.
(8) Tam, J.; Cordier, G. A.; Borbely, J. S.; Sandoval Alvarez, A.; Lakadamyali, M. *PLoS One* **2014**, *9* (7), e101772.
(9) Angelo, M.; Bendall, S. C.; Finck, R.; Hale, M. B.; Hitzman, C.; Borowsky, A. D.; Levenson, R. M.; Lowe, J. B.; Liu, S. D.; Zhao, S.; Natkunam, Y.; Nolan, G. P. *Nat. Med.* **2014**, *20* (4), 436−42.
(10) Giesen, C.; Wang, H. A.; Schapiro, D.; Zivanovic, N.; Jacobs, A.; Hattendorf, B.; Schuffler, P. J.; Grolimund, D.; Buhmann, J. M.; Brandt, S.; Varga, Z.; Wild, P. J.; Gunther, D.; Bodenmiller, B. *Nat. Methods* **2014**, *11* (4), 417−22.
(11) Levenson, R. M.; Borowsky, A. D.; Angelo, M. *Lab. Invest.* **2015**, *95* (4), 397−405.
(12) Zhang, Z.; Kenny, S. J.; Hauser, M.; Li, W.; Xu, K. *Nat. Methods* **2015**, *12* (10), 935−8.
(13) Duose, D. Y.; Schweller, R. M.; Hittelman, W. N.; Diehl, M. R. *Bioconjugate Chem.* **2010**, *21* (12), 2327−31.
(14) Schweller, R. M.; Zimak, J.; Duose, D. Y.; Qutub, A. A.; Hittelman, W. N.; Diehl, M. R. *Angew. Chem., Int. Ed.* **2012**, *51* (37), 9292−6.
(15) Zimmermann, T.; Marrison, J.; Hogg, K.; O'Toole, P. *Methods Mol. Biol.* **2014**, *1075*, 129−48.
(16) Zrazhevskiy, P.; Gao, X. *Nat. Commun.* **2013**, *4*, 1619.
(17) Jungmann, R.; Avendano, M. S.; Woehrstein, J. B.; Dai, M.; Shih, W. M.; Yin, P. *Nat. Methods* **2014**, *11* (3), 313−8.
(18) Agasti, S. S.; Wang, Y.; Schueder, F.; Sukumar, A.; Jungmann, R.; Yin, P. *Chem. Sci.* **2017**, *8* (4), 3080−3091.
(19) Jungmann, R.; Steinhauer, C.; Scheible, M.; Kuzyk, A.; Tinnefeld, P.; Simmel, F. C. *Nano Lett.* **2010**, *10* (11), 4756−61.
(20) Micheva, K. D.; Busse, B.; Weiler, N. C.; O'Rourke, N.; Smith, S. J. *Neuron* **2010**, *68* (4), 639−53.
(21) Cheng, C. L.; Djajadi, H.; Molday, R. S. *Methods Mol. Biol.* **2012**, *935*, 185−99.
(22) Swaroop, A.; Kim, D.; Forrest, D. *Nat. Rev. Neurosci.* **2010**, *11* (8), 563−76.
(23) Kim, D. S.; Ross, S. E.; Trimarchi, J. M.; Aach, J.; Greenberg, M. E.; Cepko, C. L. *J. Comp. Neurol.* **2008**, *507* (5), 1795−810.
(24) Yang, H.; Standifer, K. M.; Sherry, D. M. *J. Comp. Neurol.* **2002**, *443* (3), 275−88.
(25) Zoeller, J. J.; Bronson, R. T.; Selfors, L. M.; Mills, G. B.; Brugge, J. S. *NPJ. Breast Cancer* **2017**, *3*, 18.
(26) Viegas, M. S.; Martins, T. C.; Seco, F.; do Carmo, A. *Eur. J. Histochem.* **2007**, *51* (1), 59−66.
(27) Gustafsson, M. G.; Shao, L.; Carlton, P. M.; Wang, C. J.; Golubovskaya, I. N.; Cande, W. Z.; Agard, D. A.; Sedat, J. W. *Biophys. J.* **2008**, *94* (12), 4957−70.
(28) Guizar-Sicairos, M.; Thurman, S. T.; Fienup, J. R. *Opt. Lett.* **2008**, *33* (2), 156−8.
(29) Beater, S.; Holzmeister, P.; Lalkens, B.; Tinnefeld, P. *Opt. Express* **2015**, *23* (7), 8630−8.
(30) Zeisel, A.; Munoz-Manchado, A. B.; Codeluppi, S.; Lonnerberg, P.; La Manno, G.; Jureus, A.; Marques, S.; Munguba, H.; He, L.; Betsholtz, C.; Rolny, C.; Castelo-Branco, G.; Hjerling-Leffler, J.; Linnarsson, S. *Science* **2015**, *347* (6226), 1138−42.
(31) Lee, J. H.; Daugharthy, E. R.; Scheiman, J.; Kalhor, R.; Yang, J. L.; Ferrante, T. C.; Terry, R.; Jeanty, S. S.; Li, C.; Amamoto, R.; Peters, D. T.; Turczyk, B. M.; Marblestone, A. H.; Inverso, S. A.; Bernard, A.; Mali, P.; Rios, X.; Aach, J.; Church, G. M. *Science* **2014**, *343* (6177), 1360−3.
(32) Chen, K. H.; Boettiger, A. N.; Moffitt, J. R.; Wang, S.; Zhuang, X. *Science* **2015**, *348* (6233), aaa6090.
(33) Chen, F.; Tillberg, P. W.; Boyden, E. S. *Science* **2015**, *347* (6221), 543−8.
(34) Schueder, F.; Strauss, M. T.; Hoerl, D.; Schnitzbauer, J.; Schlichthaerle, T.; Strauss, S.; Yin, P.; Harz, H.; Leonhardt, H.; Jungmann, R. *Angew. Chem., Int. Ed.* **2017**, *56* (14), 4052−4055.
(35) Dirks, R. M.; Pierce, N. A. *Proc. Natl. Acad. Sci. U. S. A.* **2004**, *101* (43), 15275−8.
(36) Schweitzer, B.; Wiltshire, S.; Lambert, J.; O'Malley, S.; Kukanskis, K.; Zhu, Z.; Kingsmore, S. F.; Lizardi, P. M.; Ward, D. C. *Proc. Natl. Acad. Sci. U. S. A.* **2000**, *97* (18), 10113−9.
(37) Chung, K.; Wallace, J.; Kim, S. Y.; Kalyanasundaram, S.; Andalman, A. S.; Davidson, T. J.; Mirzabekov, J. J.; Zalocusky, K. A.; Mattis, J.; Denisin, A. K.; Pak, S.; Bernstein, H.; Ramakrishnan, C.; Grosenick, L.; Gradinaru, V.; Deisseroth, K. *Nature* **2013**, *497* (7449), 332−7.
(38) Murray, E.; Cho, J. H.; Goodwin, D.; Ku, T.; Swaney, J.; Kim, S. Y.; Choi, H.; Park, Y. G.; Park, J. Y.; Hubbert, A.; McCue, M.; Vassallo, S.; Bakh, N.; Frosch, M. P.; Wedeen, V. J.; Seung, H. S.; Chung, K. *Cell* **2015**, *163* (6), 1500−14.
(39) Cai, D.; Cohen, K. B.; Luo, T.; Lichtman, J. W.; Sanes, J. R. *Nat. Methods* **2013**, *10* (6), 540−7.
(40) Lichtman, J. W.; Pfister, H.; Shavit, N. *Nat. Neurosci.* **2014**, *17* (11), 1448−54.

DOI: 10.1021/acs.nanolett.7b02716
Nano Lett. 2017, 17, 6131−6139

Supporting Information

Rapid sequential *in situ* multiplexing with DNA-Exchange-Imaging in Neuronal Cells and Tissues

Yu Wang,[1,2,3,9] Johannes B. Woehrstein[1,2,15], Noah Donoghue,[1,3,13] Mingjie Dai,[1,2,10] Maier S. Avendaño,[1,2] Ron C.J. Schackmann,[4] Jason J. Zoeller, [4] Shan Shan H. Wang,[5,11] Paul W. Tillberg,[7,12] Demian Park[7], Sylvain W. Lapan[3], Edward S. Boyden,[6,7], Joan S. Brugge,[4] Pascal S. Kaeser,[5] George M. Church, [1,3] Sarit S. Agasti,[1,2,14,*], Ralf Jungmann,[1,2,15*] Peng Yin.[1,2,*]

1. Wyss Institute for Biologically Inspired Engineering, Harvard University, Boston, Massachusetts, 02115, USA.
2. Department of Systems Biology, Harvard Medical School, Boston, Massachusetts, 02115, USA.
3. Department of Genetics, Harvard Medical School, Boston, Massachusetts, 02115, USA.
4. Department of Cell Biology, Harvard Medical School, Boston, Massachusetts, 02115, USA.
5. Department of Neurobiology, Harvard Medical School, Boston, Massachusetts, 02115, USA.
6. Department of Biological Engineering, Massachusetts Institute of Technology (MIT), Cambridge, Massachusetts, 02139, USA.
7. Media Lab, MIT, Cambridge, Massachusetts, 02139, USA.
8. Department of Brain and Cognitive Sciences, MIT, Cambridge, Massachusetts, 02139, USA.
9. Program in Biological and Biomedical Sciences, Harvard Medical School, Boston, Massachusetts, 02115, USA.
10. Program in Biophysics, Harvard University, Boston, Massachusetts, 02138, USA.
11. Program in Neuroscience, Harvard Medical School, Boston, Massachusetts, 02115, USA.
12. Department of Electrical Engineering and Computer Science, MIT, Cambridge, Massachusetts 02139, USA.
13. Warren Alpert Medical School, Brown University, Providence, Rhode Island, 02903, USA.
14. Present address: New Chemistry Unit and Chemistry & Physics of Materials Unit, Jawaharlal Nehru Centre for Advanced Scientific Research (JNCASR), Bangalore, India.
15. Present address: Department of Physics and Center for Nanoscience, Ludwig Maximilian University, 80539 Munich, Germany, Max Planck Institute of Biochemistry, 82152 Martinsried near Munich, Germany.
*Emails: P.Y. (py@hms.harvard.edu; 617-432-7731), R.J. (jungmann@biochem.mpg.de), and S.S.A. (sagasti@jncasr.ac.in)

Methods

Cultured cells preparation and staining

All animal procedures were in accordance with the National Institute for Laboratory Animal Research Guide for the Care and Use of Laboratory Animals and approved by the Harvard Medical School Committee on Animal Care and the Massachusetts Institute of Technology Committee on Animal Care.

Hippocampal neuron cultures were prepared from postnatal day 0 or 1 mice and plated on eight-well Lab-Tek II chambers with a density of 10,000 ~ 15,000 cells per well. Cells were grown for 14 days before fixation. Neurons used in Figure 2 were fixed using precooled methanol at -80 °C followed by three 5 minute PBS washes. Neurons used in other figures were fixed using 4% formaldehyde for 15 minutes at 37 °C, followed by quenching in 50 mM NH_4Cl for 10 minutes. HeLa cell and BSC1 cells were plated on eight-well Lab-Tek II chambers (15,000 cells per well) and grown for 24 hours. BSC1 cells used in SIM experiments were fixed using 3% Paraformaldehyde (PFA), 0.1% Glutaraldehyde, and 0.1% Triton X-100 for 12 minutes. Cells used in other experiments were fixed with 4% PFA.

Cells were then permeabilized and blocked in 0.1% Triton X-100, 0.1% Tween20, 3% Acetyl-BSA and 5% normal donkey serum for 2 hours. Specimens were incubated with primary antibodies diluted in incubation buffer (0.1% Triton X-100, 0.1% Tween20, 3% IgG-free BSA) overnight at 4 °C, and then washed with washing buffer (0.1% Tween20, 1% IgG-free BSA) for five times (brief wash for the first two washes and 10 minute incubation for the other three washes). DNA-labeled secondary antibodies (Jackson ImmunoResearch, conjugated in house) diluted in incubation buffer were incubated with samples for 2 hours at room temperature and then washed as for primary antibodies. In multiplexed detection experiment in which primary antibody-DNA docking strand conjugates were used, the sample was left on the microscope to maintain the position for imaging. Conjugated primary antibodies were diluted in incubation buffer and incubated with samples for 2 hours at room temperature, followed by PBS wash as described above. Post-staining fixation using 4% paraformaldehyde for 10 minutes followed by 5 minute quenching is recommended but optional.

Brain tissue preparation and staining

Transgenic mice expressing cytosolic YFP under the Thy1 promoter (Thy1-YFP-H C57BL/6 strain) were anesthetized with isoflurane and perfused transcardially with ice cold 4% paraformaldehyde. Dissected brains were kept in 4% paraformaldehyde at 4 °C for 24 hours, and then sunk in 30% sucrose with 100 mM glycine for 24 hours. Brains were sliced into 6 μm slices on a cryotome (Leica CM1850UV). Slices were kept in PBS at 4 °C until mounted on No 1.5 coverslips. Brain slices were permeabilized and blocked with 0.1% Triton X-100, 0.1% Tween20, 3% Acetyl-BSA, 5% normal donkey serum and a mixture of polydT DNA (20, 25, 30, 40 mers with 1 μM for each) overnight at 4 °C. Primary antibodies were diluted in incubation buffer as for neuron culture and incubated with brain slices for 48 hours at 4 °C. Slices were then washed using washing buffer three times for thirty minutes each. Slices were then incubated with secondary antibodies that were diluted in incubation buffer for overnight at 4 °C, followed by washing as for primary antibodies.

Mouse retina section preparation and staining

Animals were given a lethal dose of sodium pentobarbital (120 mg/kg) (MWI, 710101) and enucleated immediately. Eyes were removed and fixed in PFA for 15-30 min. Following dissection, retinas were immersed in 30% sucrose overnight prior to freezing in TFM (EMS, 72592) and cryosectioning at 40 μm. Coverslips were treated with poly-D-Lysine overnight, followed by PBS washes. Retina sections were washed with PBS + 0.3% Triton X-100 for three times with five minutes per wash. They were then blocked and stained as above. Note that SV2 was stained using DNA-primary antibody conjugates whereas other targets were stained using primary antibodies followed by DNA-secondary antibody conjugates.

Breast tumor section preparation and staining

Ductal carcinoma *in-situ* tumors were generated using the SUM225 cell line as described previously[1]. Tumor tissues were formalin fixed and paraffin embedded. 4 μm sections were mounted onto coverslips (24 × 50 mm no.1.5 VWR #48393.241) pre-treated with Silane solution (Leica Biosystems #3803120) to prevent tissue detachment during processing. Slides were baked for 1 hour at 60 °C, followed by deparaffinization in 100% xylene (Sigma 534056) for 5 minutes twice, and rehydrated by ethanol series (2 time for 2 minutes each 100% with EtOH, 1 time for 2 minutes with 70% EtOH, 1 time for 2 minutes with 50% EtOH, 1 time for 2 minutes with 25% EtOH, 1 time for 5 minutes with ddH_2O). The coverslips were incubated in antigen retrieval solution (IHCworld Cat# IW-1100) and placed in a steamer (Black & Decker HS1050) for 40 minutes (cold start). Slides were allowed to cool to room temperature for 20 minutes, followed by two washes of 5 minutes in ddH_2O. Blocking was performed using 5% goat serum (invitrogen #16210) in 1× Tris-buffered saline (TBS) for 30 minutes at room temperature. Tissue sections were incubated in TBS with

2.5% goat serum containing anti-HER2 and anti-SMA primary antibodies for 1 hour at room temperature. Slides were incubated with DNA-conjugated secondary antibodies for 1 hour at room temperature and stored in TBS until imaging.

Diffraction-limited image acquisition

The diffraction-limited images in Figure 2, Figure 3c and Figure S1-3, 6 and 10 were acquired with a Yokogawa spinning disk confocal CSU-X1 unit on a Nikon Ti inverted microscope. Figure 2 and Figure S1-3 and 10 were acquired using a 100× Plan Apo NA1.4 oil-immersion objective whereas Figure 3c and Figure S6 were acquired using a 20× / 0.75 NA dry objective with additional 1.5× magnification. Alexa488 was visualized using the 488 nm laser (1.74 mW, out of objective) and 525/50 emission filter; YFP was visualized using the 515 nm laser (1.89 mW) and 535/30 emission filter; Cy3b was visualized using 561 nm laser (4.02 mW) and 620/60 emission filter; Atto655 was visualized by the 647 nm laser (7.2 mW) and 700/75 emission filter. Images were collected with an ORCA-AG cooled CCD camera from Hamamatsu and Metamorph software. Camera exposure time was kept at 5 seconds for Figure 2 and 0.75 second for Figure 3. Z-stacks were collected with a z-step size of 140 nm for Figure 2.

In Figure 2, SynapsinI, vGAT, MAP2, pNFH and AlphaTubulin were stained using primary antibodies from five species, followed by DNA-conjugated secondary antibodies. After imaging, two primary antibodies that are directly conjugated with DNA docking strands were introduced to target AcetylTubulin and GFAP, surpassing the limitation of available antibody species. Sequential imager strand application was performed manually with gel-loading tips. Imager strands were diluted in 1× PBS/ 500 mM NaCl with a concentration of 10 nM. 1× PBS with 0.1% Tween 20 was used as washing buffer to remove imager strands.

The images in Figure 3a and b and Figure S4, 11 were acquired using a Zeiss Axio Observer with LSM 710 scanning confocal system. The images were 1024*1024 pixels and acquired at acquisition speed 7. Each image was acquired by averaging 4 images. The retina multiplexing experiment was performed by six rounds of buffer exchange of Cy3b-tagged imager strands. The laser intensity and exposure time were kept the same for the negative control group and experiment group in Figure S4. The scale was adjusted to the same range using FIJI for comparison. To facilitate imager strand removal in thick tissue sample, 0.1× PBS with 0.1% Tween 20 was used as washing buffer in the exchange tissue imaging experiment.

Multiplexed Structured Illumination image acquisition

BSC1 cells grown in Lab-Tek chambers were fixed and stained with primary antibodies targeting alphaTubulin, betaTubulin, Tom20 and Vimentin, followed by DNA-conjugated secondary antibodies. Alexa488-conjugated anti-chicken (Vimentin) secondary antibodies was added along with DNA-conjugated secondary antibodies in about 1:10 ratio (dye conjugated and DNA-conjugated anti-chicken antibodies). Antibodies were fixed using 4% PFA after staining. The multiplexed images were acquired by four rounds of buffer exchange of Cy3b-tagged imager strands. All 3D-SIM data was collected on a Zeiss ELYRA system with a 63×/1.40 N.A Plan Apo oil immersion objective lens. Image stacks were acquired with a z-step of 150 nm and with 25 raw images per plane (five phases and five angles). Super-resolution images were computationally reconstructed from the raw data set with a built-in algorithm in the Zeiss software. Buffer exchange was performed using flow cell chambers described in Jungmann and Avendaño et al.[2]. Glox oxygen scavenger system was added to the imaging buffer to prevent photobleaching. 0.1× PBS was used as washing buffer to facilitate imager strand removal.

Multiplexed STED image acquisition

Images were acquired using Leica SP8 X with STED 3X microscope system. Leica 100X/1.4 oil objective specialized for STED imaging is used. Green and Red channel laser/detection were set up as 488 nm/(500-540 nm) and 561 nm/(570-630 nm). Imaging was performed at zoom 5 with 1024 × 1024 format, yielding 23 nm pixel size to match STED imaging resolution requirement. Multiple

line accumulation and frame average were used to increase STED image Signal-to-Noise quality. SynapsinI was stained also with Alexa488-conjugated secondary antibodies and its signal from 488 nm laser channels were used for image registration.

Super-resolution Exchange-PAINT image acquisition

Images were acquired using an inverted Nikon Eclipse Ti microscope, applying an objective-type TIRF configuration using a Nikon TIRF illuminator with a 100×, NA1.49 oil-immersion objective (CFI Apo TIRF). Two sets of lasers and emission filters were used: 488 nm (200 mW nominal, Coherent Sapphire) / ET525/50 nm and 647 nm (300 mW nominal, MBP Communications) / ET700/75 nm. Images were captured on an electron-multiplying (EM) CCD camera (iXon X3 DU-897, Andor Technologies). The CCD readout rate was set to 3 MHz at 16 bit and 5.1 pre-amp gain. No EM gain was used. 30,000 frames with 100 ms integration time were acquired for each target. 80 nm gold nanospheres (Microspheres-Nanospheres) were used as fiducial markers for drift and alignment markers. The z-axis focal planes were kept constant for all the synaptic proteins, SynapsinI, Bassoon, vGAT and Gephyrin, while the focal planes were adjusted for four other structural proteins to obtain images of optimal quality. Sequential imager strand application was performed manually with gel-loading tips. Imager strands were diluted in 1× PBS/ 500 mM NaCl with a concentration of 3 nM. 1× PBS with 0.1% Tween 20 was used as washing buffer to remove imager strands.

Image processing and analysis

For super-resolution PAINT images, the time-lapse imaging movies were saved as Raw Data using FIJI and imported into custom-written program in MATLAB. The final images were reconstructed using spot-finding and 2D-Gaussian fitting algorithms. A simplified version of this software is available for download at http://molecular.systems/software or http://www.dna-paint.net. The image alignment for the merged synaptic protein image was performed by overlaying gold nanoparticles manually.

Image registration for diffraction-limited data acquired by the spinning disk confocal microscope was performed as follows: since samples were maintained on the stage and all microscope settings were kept the same during the entire experiment, only rigid transformation (translation and rotation) will be considered and corrected. The spinning disk confocal microscope contained the Nikon perfect focus system to maintain z-position. Therefore, drifts in only x- and y-axis were corrected. Signals from 488 nm laser channel were captured in every exchange cycle and served as the reference for sample drift. Images were first corrected for translation using a Fast Fourier Transformation (FFT)-based phase correlation algorithm, and then corrected for rotation using a Harris feature extraction and matching algorithm with Matlab built-in functions. The transformation matrices were applied to target images.

Image registration for 3D diffraction-limited retina imaging was performed using an algorithm developed by Hunter Elliott from Harvard Medical School Image and Data analysis core. The images were first filtered with a gradient filter and the intensity was then normalized. 3D FFT- based phase correlation was performed to calculate the image shift.

Subpixel Image registration for SIM and STED was performed based on an algorithm developed by Guizar-Siciros M, et al.[3] (the Matlab code is available from Mathworks and the detailed algorithm was described in the original paper). The initial code was written for 2D image registration but it can be extended to 3D by adding one dimension. For 3D SIM data, the reference image f and target image g were first converted to frequency domain F and G using FFT. The normalized cross-spectrum is defined as $R = F \times G^* / |F \times G^*|$, where G^* denotes the complex conjugate of G. To have an upsampling factor of 2, R was zero padded into a larger array of dimension (2x, 2y, 2z). This number can be further increased. However, it can be very computationally expensive. Further upsampling was achieved in the 1.5x1.5 pixel region of the estimated peak of cross-correlation using matrix multiplication discrete Fourier Transformation. For STED data, only 2D image registration was performed using the same method.

Cross correlation studies for Figure 2 and Figure S3 were performed using normxcorr2 function in Matlab.

Antibody-DNA conjugation

The conjugation involves crosslinking of thiol-modified DNA oligonucleotidess to Lysine residues on antibodies[4]. In brief, 250 uM 5' thiol-modified DNA oligonucleotides (Integrated DNA Technologies) were activated by 100 mM DTT for 2 hours and then purified using NAP5 columns (GE Healthcare Life Sciences, 17-0853-02) to remove excessive DTT. Antibodies formulated in PBS only were concentrated using 100KDa Ambicon Ultra Filters (EMDMillipore, UFC510096) to 2 mg/ml and reacted with maleimide-PEG2-succinimidyl ester crosslinkers (Singma 746223) for 2 hours. Antibodies were then purified using 0.5ml 7kDA Zeba desalting columns (LifeTechnologies, 89883) to remove excessive crosslinkers. Activated DNA oligonucleotides were incubated with antibodies (11:1 DNA: Antibody ratio) overnight at 4 °C. Final conjugated antibodies were washed using PBS/BSA (100ug/ml) in Ambicon Ultra Filters four times to remove nonreacted DNA oligonucleotides. Conjugated antibodies were kept at 4 °C.

The SV2 antibody used in Figure 3 was conjugated using the SiteClick kit from ThermoFisher (S10467). The DBCO-modified DNA oligos were purchased from Boston Open Labs.

Supplementary Figures and Tables

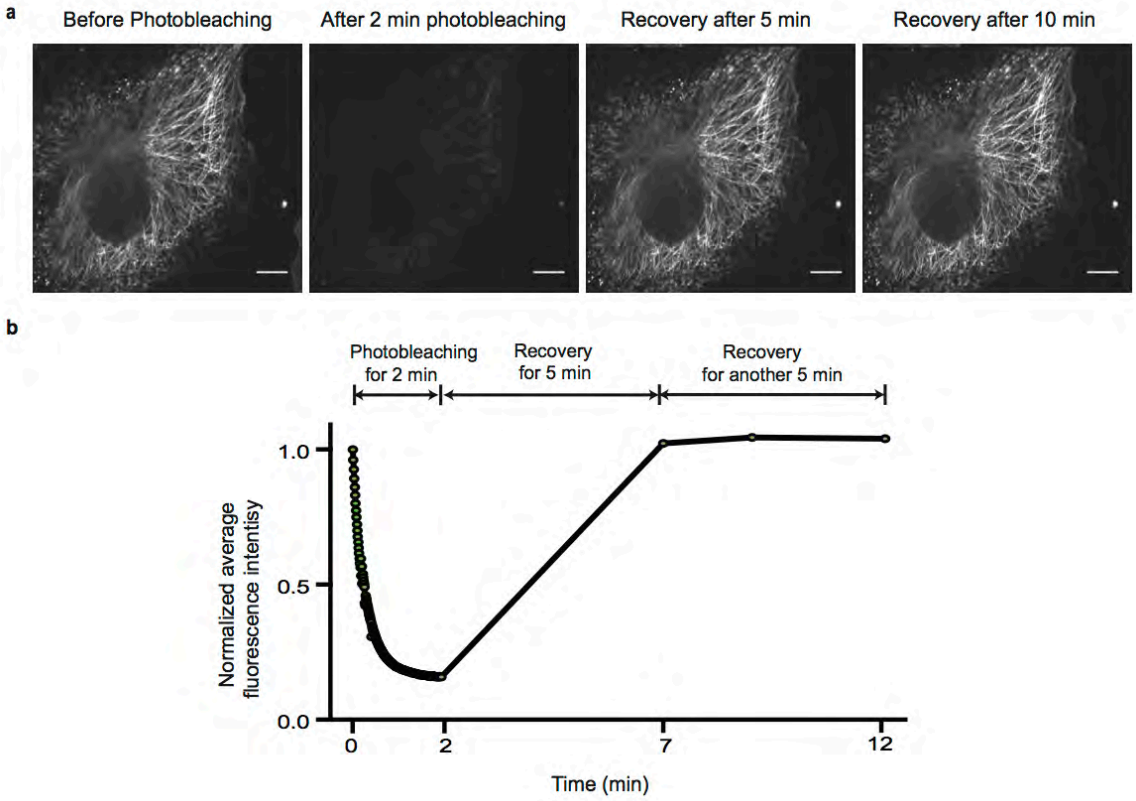

Figure S1. Fluorescent signal recovery after photobleaching in DNA-Exchange-Imaging. (**a**) BSC1 cells were stained for Beta-tubulin and imaged using Cy3b-conjugated imager strands. Photobleaching was performed using a 561 nm laser with 30 mW excitation power. Fluorescence signal decreased after photobleaching. A series of 200 images were taken in 2 min with 600 ms camera exposure time for each image. Fluorescence was then allowed to recover for 10 min. (**b**) Quantification of average fluorescence intensity of the images. The average fluorescence intensity dropped to 16% after 2 min of photobleaching and returned to ~100% after 5 minutes and remained the same afterwards.

Note: Fluophores can be typically photobleached upon sufficient long exposure to excitation lasers, and the rate of photobleaching depends on fluorophore species, the intensity of illuminating lasers and the buffer environment. Initial focusing and scanning of the specimen to locate the regions of interest often results in photobleaching of the fluorophores and hence undesired loss of fluorescent signals. Using conventional imaging methods with dye-conjugated antibodies, photobleaching is not reversible and leads to permanent loss of fluorescence signals. However, in DNA-Exchange-Imaging, due to the semi-transient nature of the binding interaction between the imager strand and docking strand, a photobleached imager strand will be eventually replenished by an unbleached one in the solution, allowing the full recovery of transiently bleached fluorescence signals at the target site. Scale bars: 10 μm.

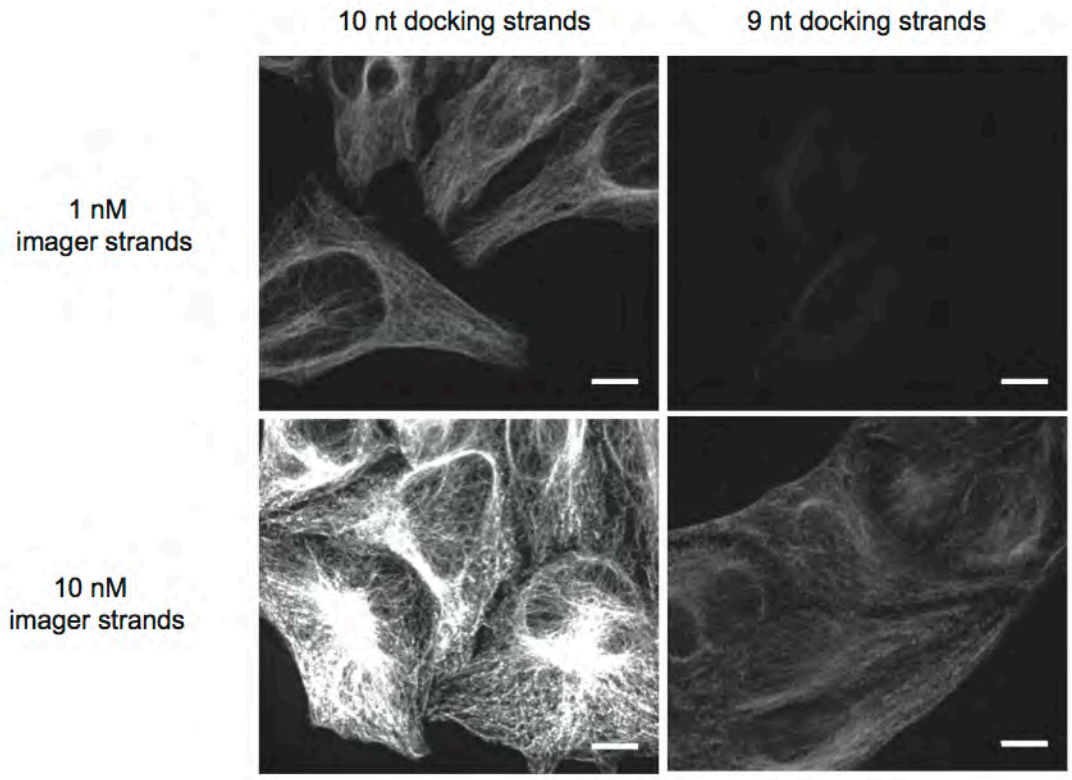

Figure S2. Comparison of image quality between 9 nucleotides (9 nt) DNA docking strands and 10 nucleotides (10 nt) DNA docking strands at different imager strand concentrations. Microtubules in HeLa cells were targeted using a rat alphaTubulin primary antibody. A donkey anti-rat secondary antibody, tagged with 9 nt docking sequence (Ab-TTGATCTACAT) or 10 nt (Ab-TTGATCTACATA) docking sequence, was used for indirect immunostaining. The sequence for imager strand is TATGTAGATC-dye. In diffraction-limited imaging, 10 nt docking strands perform significantly better than 9 nt. All images were taken using the same laser intensity and camera exposure time, and presented in the same scale for brightness. Scale bars: 10 μm.

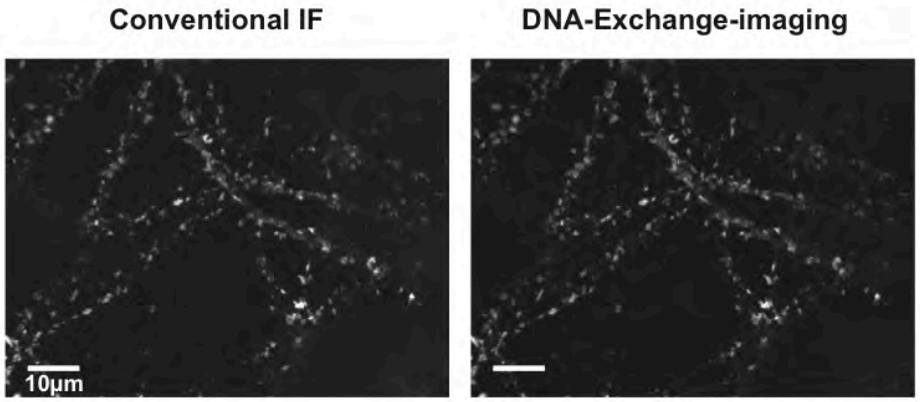

Figure S3. Comparison of SynapsinI signal imaged using conventional IF imaging and DNA-Exchange-imaging. Fixed DIV14 mouse hippocampal neurons were stained with SynapsinI primary antibodies, followed by both Alexa488-conjugated and DNA docking strands conjugated secondary antibodies (Ab-TTATGAATCTAC) as in the schematic. Images on the left were from conventional IF imaging taken with the 488nm laser channel. Images on the right were from DNA-Exchange-imaging taken with Cy3b-tagged imager strands under the 561 nm laser channel. Scale bars: 10 μm. Correlation Coefficient: 0.9607.

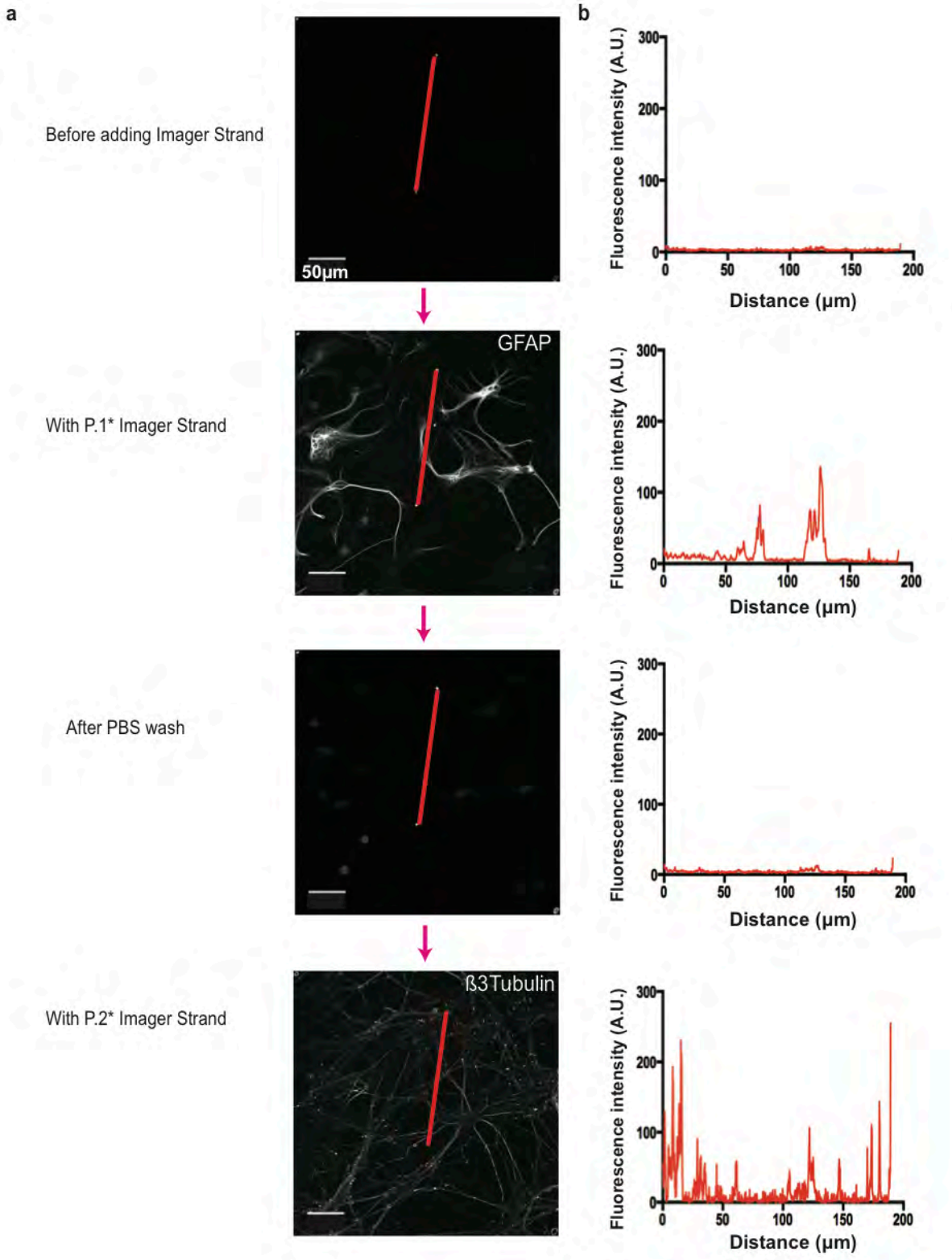

Figure S4. Efficiency of imager strand removal between imaging cycles based on fluorescence intensity measurement. Fixed DIV14 mouse hippocampal neurons were stained with antibodies targeting GFAP and beta3Tubulin. **(a)** P.1* imager strands (TATGTAGATC-Cy3b) were firstly introduced to specifically visualize GFAP followed by PBS wash for 5 minutes. P.2* imager strands (GTAATGAAGA-Cy3b) were then introduced to visualize beta3Tubulin. All images were adjusted to the same brightness scale. Scale bars: 50 μm. **(b)** Fluorescence intensity along the red line shown in (a).

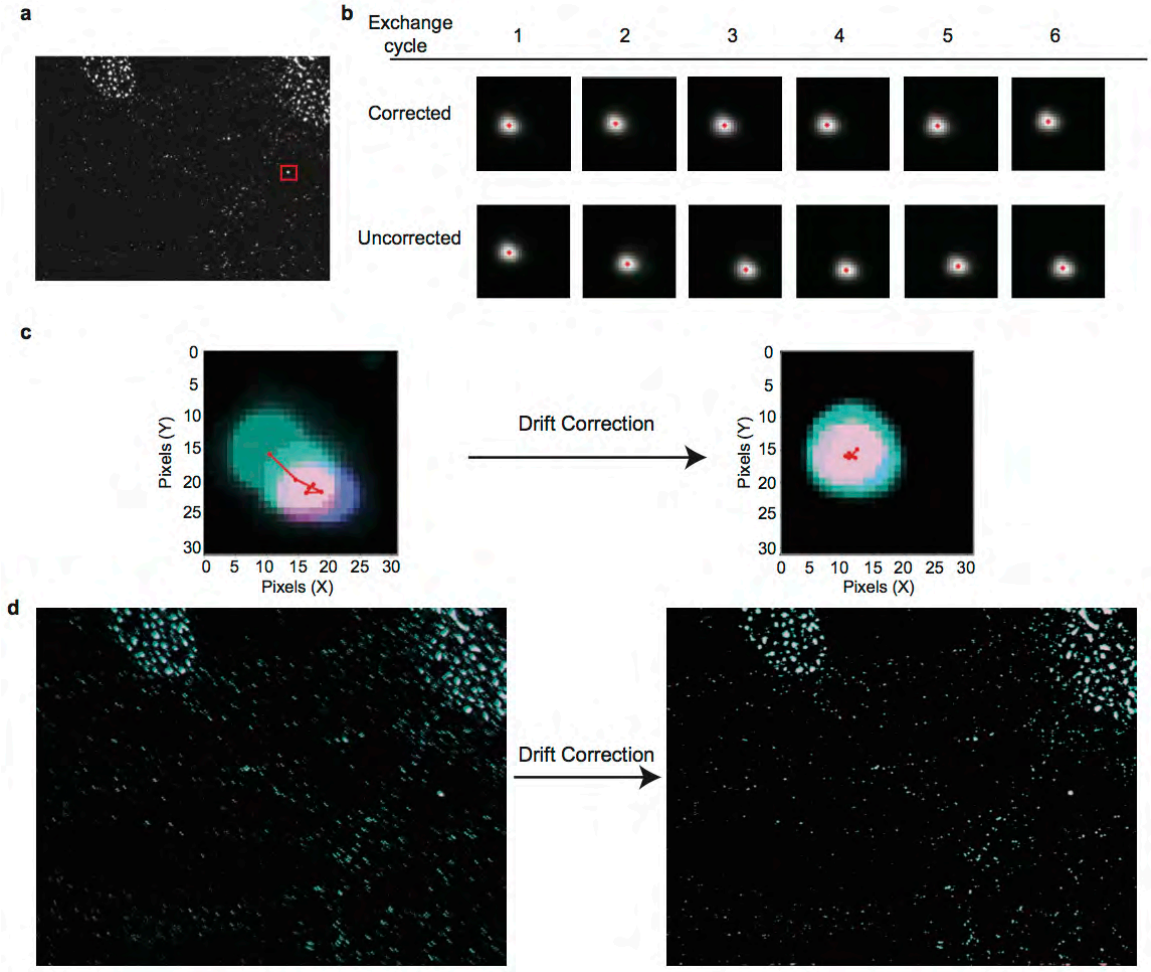

Figure S5. Drift correction of multiplexed diffraction-limited DNA-Exchange-imaging results from Figure2. (a) Images on 488 nm laser channel (stained using gephyrin primary antibodies followed by Alexa488-labeled secondary antibodies in this experiment) were imaged on every cycle of imaging along with other targets. The bright signal indicated in the red box region was used for demonstration in (b) and (c). **(b)** Comparison of the centroid positions of the selected marker in drift-corrected and uncorrected images from six cycles of imager strand exchange. The centroids were marked as red asterisks. **(c)** Track of centroid positions of the selected marker in merged images from (b). The x- and y- axis indicted the pixel value, and the whole image is 31 × 31 pixels with a pixel size of ~ 64 × 64 nm^2. **(d)** Comparison of uncorrected and corrected images.

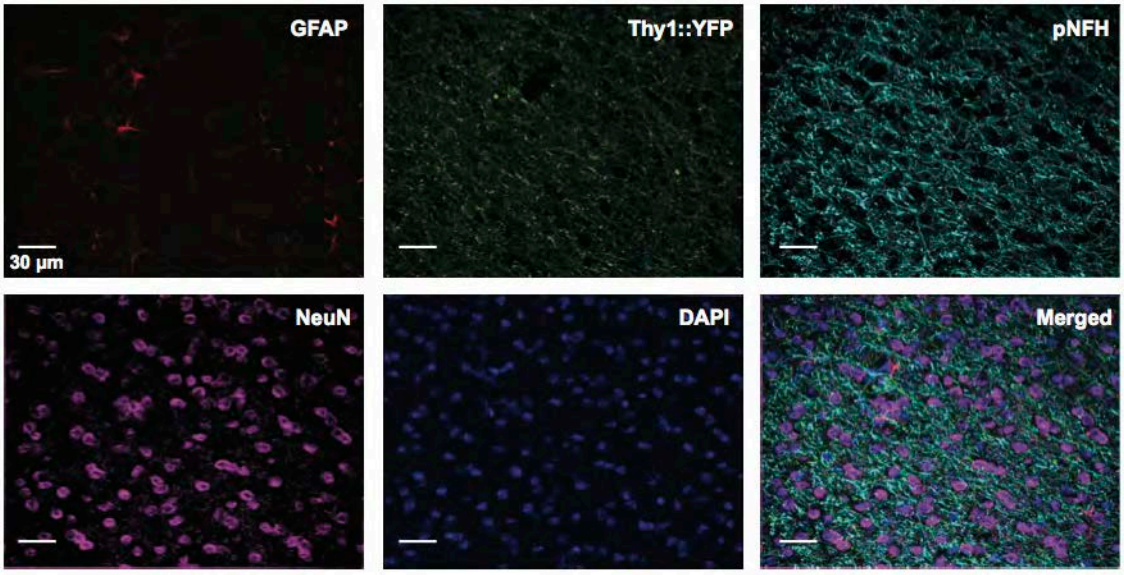

Figure S6. Five-target multiplexed diffraction limited imaging of mouse brain tissue sections. A 10 µm-thick mouse cortex section expressing Thy1::YFP was stained for GFAP, YFP, pNFH and NeuN. 2D images were taken using four rounds of exchange with Cy3b-tagged imager strands. The nucleus was stained with DAPI. Scale bars: 30 µm. DNA docking strand sequences are listed in **Table S6**.

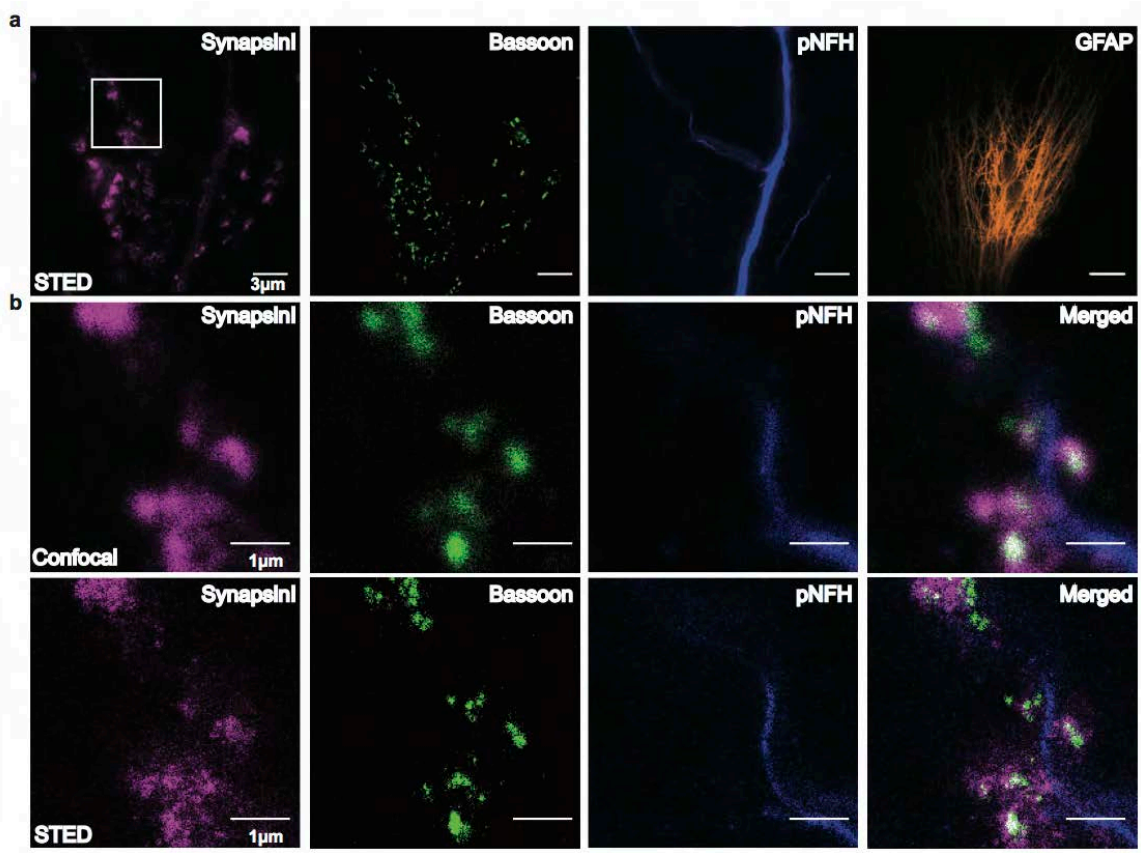

Figure S7. Multiplexed chromatic aberration-free Stimulated emission depletion (STED) imaging using DNA-Exchange-imaging. (a) Fixed DIV14 mouse hippocampal neurons were stained for GFAP, pNFH, SynapsinI and Bassoon. Four-round exchanges of Cy3b-conjugated imager strands were performed to acquire a 2D image for each target. It should be noted that GFAP was imaged in a region slightly under the other three targets because of the missing GFAP signal in the original region. Scale bar: 3 µm. **(b)** Magnified view of SynapsinI, Bassoon and pNFH from the white square region in (a). Confocal images of the same region are also presented for comparison. Scale bar 1 µm. DNA docking strand sequences are listed in **Table S9**.

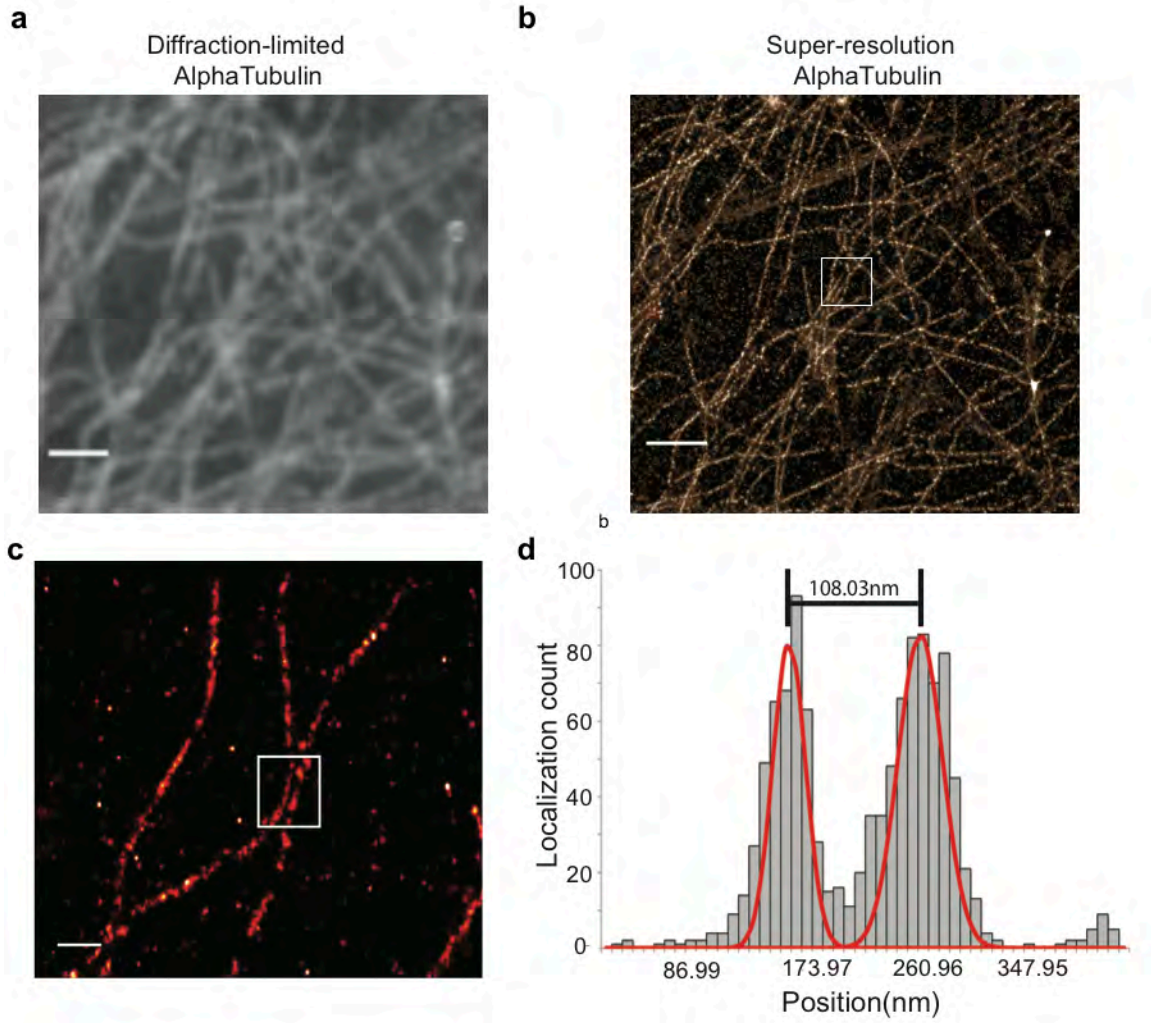

Figure S8. Super-resolved microtubule structure imaged with DNA-PAINT. (a) and **(b)** Comparison of diffraction-limited (a) and super-resolution (b) images of microtubules from Figure 5. Scale bar: 2 μm. **(c)** A magnified region from (b), where the region of analysis is indicated by a white box. Scale bar 500 nm. **(d)** Cross-sectional histogram of highlighted region in (c). The distance of the two microtubules is ~108 nm, well below the diffraction limit. The FWHM for the two microtubules are 44.8 nm and 68.0 nm, respectively.

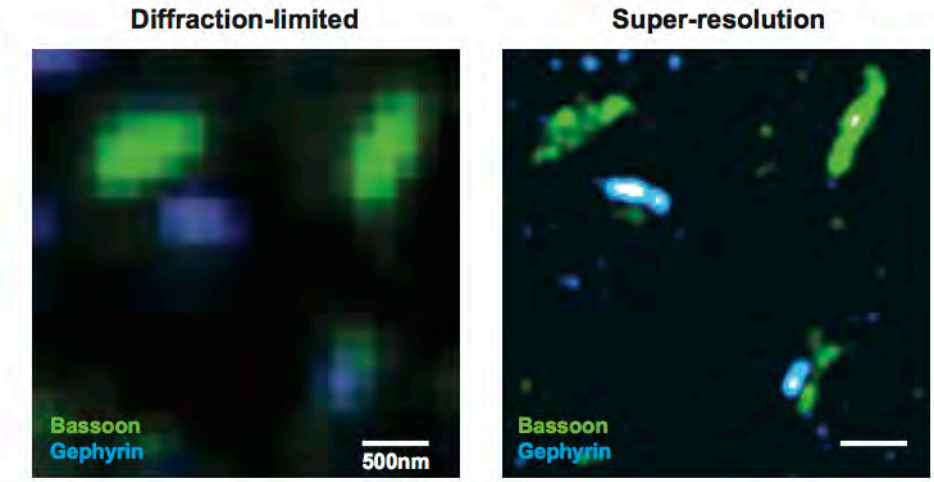

Figure S9. Visualization of presynaptic and postsynaptic proteins in diffraction-limited and super-resolved images. The left panel shows the view of Bassoon (presynaptic; Green) and Gephyrin (postsynaptic; Blue) in a diffraction-limited image. Bassoon and Gephyrin signals are not able to be separated. The right panel shows the view of Bassoon and Gephyrin in a super-resolved image where the signals are clearly distinguishable between the two. Scale bars: 500 nm.

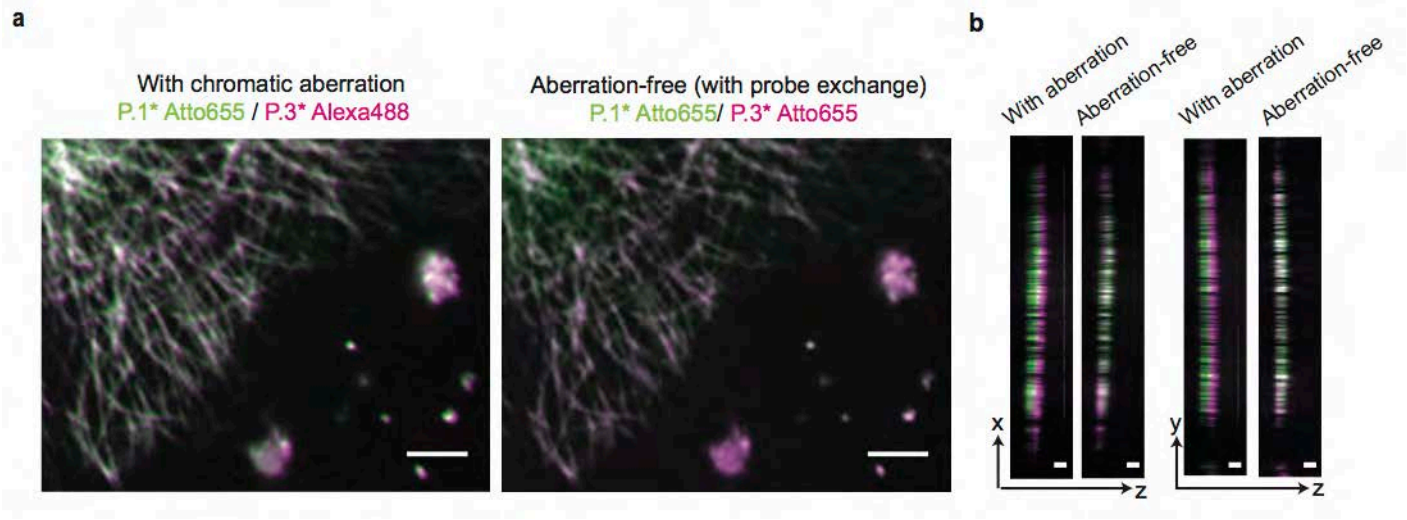

Figure S10. **Chromatic aberration-free imaging with DNA-Exchange-Imaging.** (**a**) Images with (left) and without (right) chromatic aberration. BSC1 cells were stained with primary antibodies against betaTubulin followed by two secondary antibodies, one with P.1 docking strands (Ab-TTATACATCTA) and the other one with P.3 docking strands (Ab-TTTCTTCATTA). The image with chromatic aberration was taken by addition of Atto655-conjugated P.1* imager strands and Alexa488-conjugated S.3* imager strands at the same time, whereas the image without chromatic aberration was taken by sequential addition of Atto655-conjugated P.1* and Atto655-conjugated P.3* imager strands. A z-stack of 101 images, each slice spaced 100 nm apart, covering ~10 µm z depth was acquired and subsequently projected onto a 2D plane for representation. An aberration-uncorrected 40× Plan Fluo lens was used in the experiment. In the image with chromatic aberration, although the target was the same, images for P.1 and P.3 docking sites that were taken using two laser channels (642 nm for Atto655 dye and 488 nm for Alexa488 dye) were shifted from each other. In contrast, DNA-Exchange-Imaging allows the two types of docking strands to be imaged using imager strands conjugated to the same species of dye (Atto655). As a result, the chromatic aberration was avoided and no shift was observed. It should be noted that any drift caused by buffer exchange in DNA-Exchange-Imaging was corrected using a reference image. In this experiment, the reference image was betaTubulin signal taken from 488 nm laser channel. That is, in the first round of imaging, Atto655-P.1* and Alexa488-P.3* were added and images were acquired for both channels; in the second round of imaging, Atto655-P.3* and Alexa488-P.3* were added and images were acquired for both channels. The drift was calculated using an algorithm to perform cross-correlation of the two reference images from the Alexa488 channel, and the images from the Atto655 channel were shifted based on the calculated drift from reference images. Scale bars 5 µm. **(b)** z axial chromatic aberration comparison between images with and without chromatic aberration. Scale bar: 2 µm (the scale bar is for Z direction only as the z pixel size is 100 nm, i.e. same with sampling spacing, and the XY pixel size is 107 nm).

Note: Chromatic aberration is caused by the failure of lens to focus light of different wavelengths to the same convergence point. Chromatic aberration can cause the same object to appear at different locations when imaged using lasers with different excitation wavelengths. DNA-Exchange-Imaging uses only one fluorophore species and hence only one excitation laser to visualize all targets, and thus naturally avoids chromatic aberration for multiplexed imaging. It should be noted that certain lenses, for example Apochromat, have been designed to correct aberration. Unfortunately, the aberration cannot be completely eliminated and may cause problems when dyes with significant spectral difference (for example, 405 nm and 647 nm) are used in the same experiment. The problem can be exacerbated if an aberration-corrected lens is not available. However, we also note that aberrations can – in principle – be "calibrated" and corrected using fluorescent beads imaged at different wavelength and subsequent nonlinear affinity matrices can

be used to "map" different wavelengths onto each other. Compared with these alternative methods for aberration correction, DNA-Exchange-Imaging is unique in that it is naturally aberration-free.

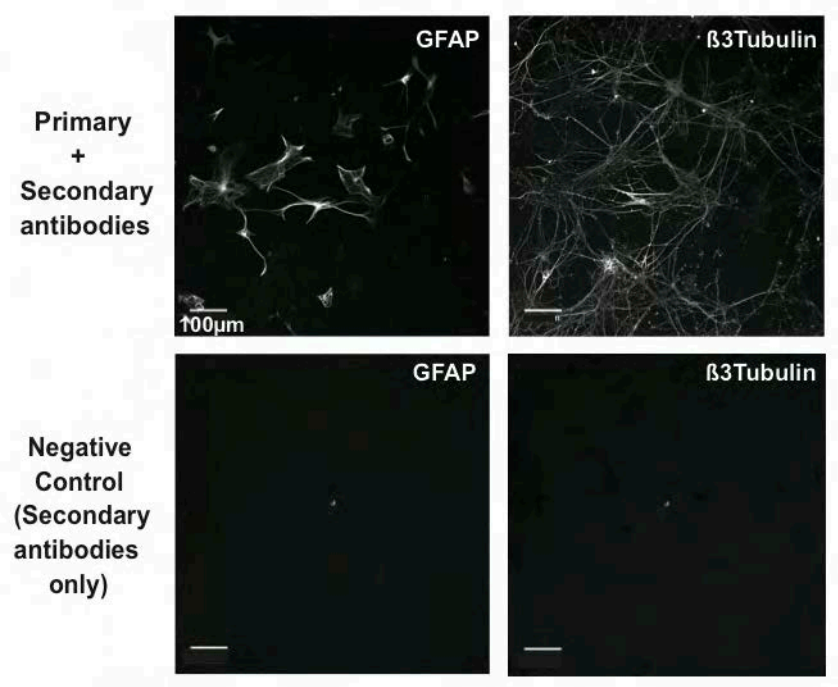

Figure S11. Test fluorescent signals caused by non-specific binding of DNA-conjugated secondary antibodies and fluorophore-conjugated imager strands. Fixed DIV14 mouse hippocampal neurons were stained with or without GFAP and beta3Tubulin primary antibodies, followed by DNA-conjugated secondary antibodies (Ab-TTATCTACATA for GFAP; Ab-TTTCTTCATTA for beta3Tubulin). The upper panel shows images taken from the sample stained with both primary and secondary antibodies, clearly distinguishing astrocytes and neurons. The lower panel shows images from the sample stained with secondary antibodies only, where no obvious signal can be observed. The laser intensities, camera exposure time and brightness scale were kept the same between two samples. Scale bar: 100 μm.

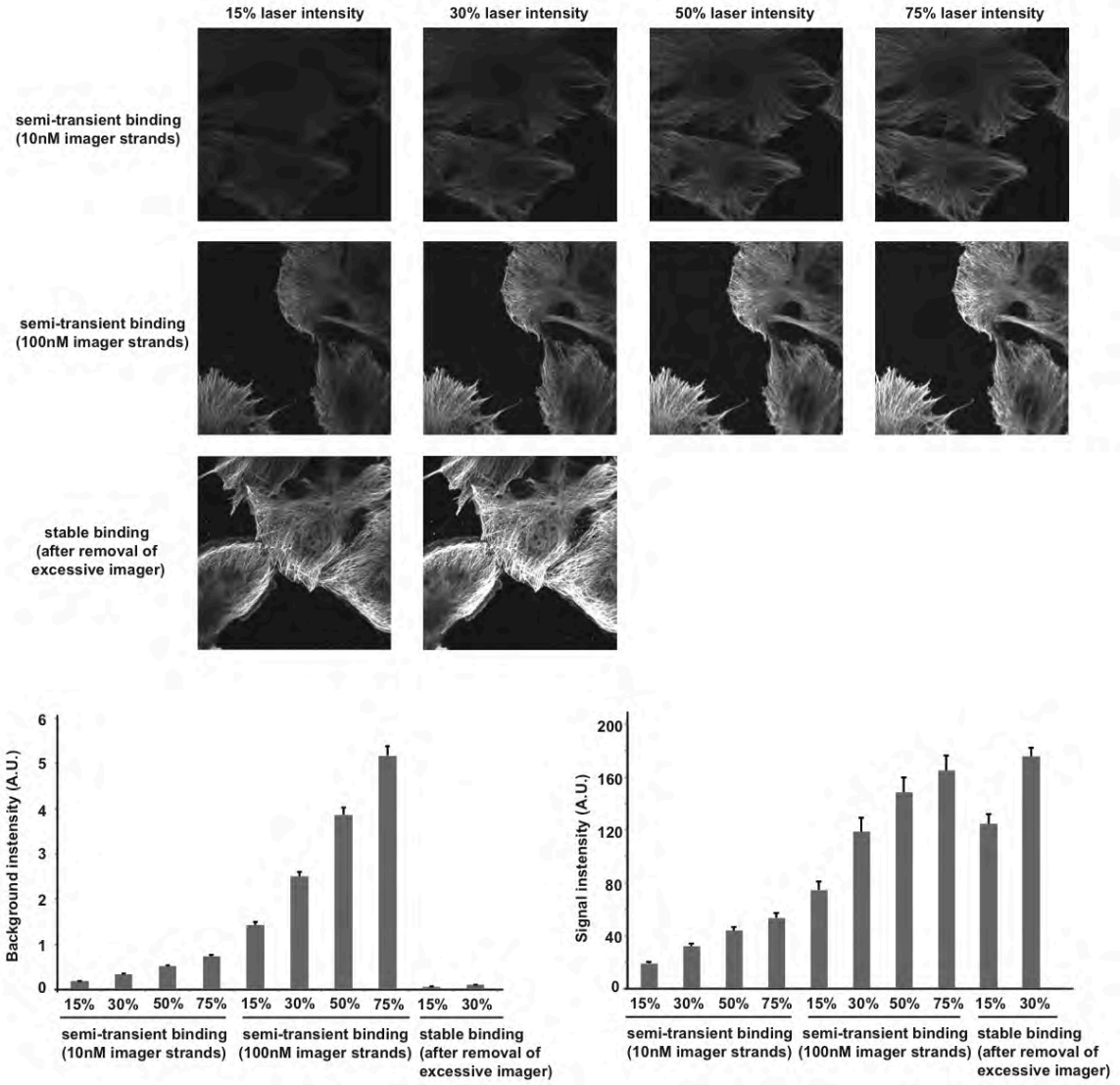

Figure S12. Comparison of imaging quality between semi-transient binding and stable binding schemes with microtubule targets. BSC1 cells were fixed and labeled with antibodies targeting Beta-Tubulin. Antibodies were conjugated with either 10-mer docking strands for semi-transient binding or 12-mer docking strands for stable binding (strand 1 used in Schueder et al.). For semi-transient binding, we added 10 nM or 100 nM Alexa647-imager strands for imaging. For stable-binding, we incubated the cells with 1μM Alexa647-imager strands for 1 hour followed by 3 times buffer washing with 5 minutes for each to remove excessive imager strands. The laser intensity was set to 15%, 30%, 50% or 75% with gain 600. All 8-bit images were displayed with the same scale of 0-255. The error bar is SEM, n = 6.

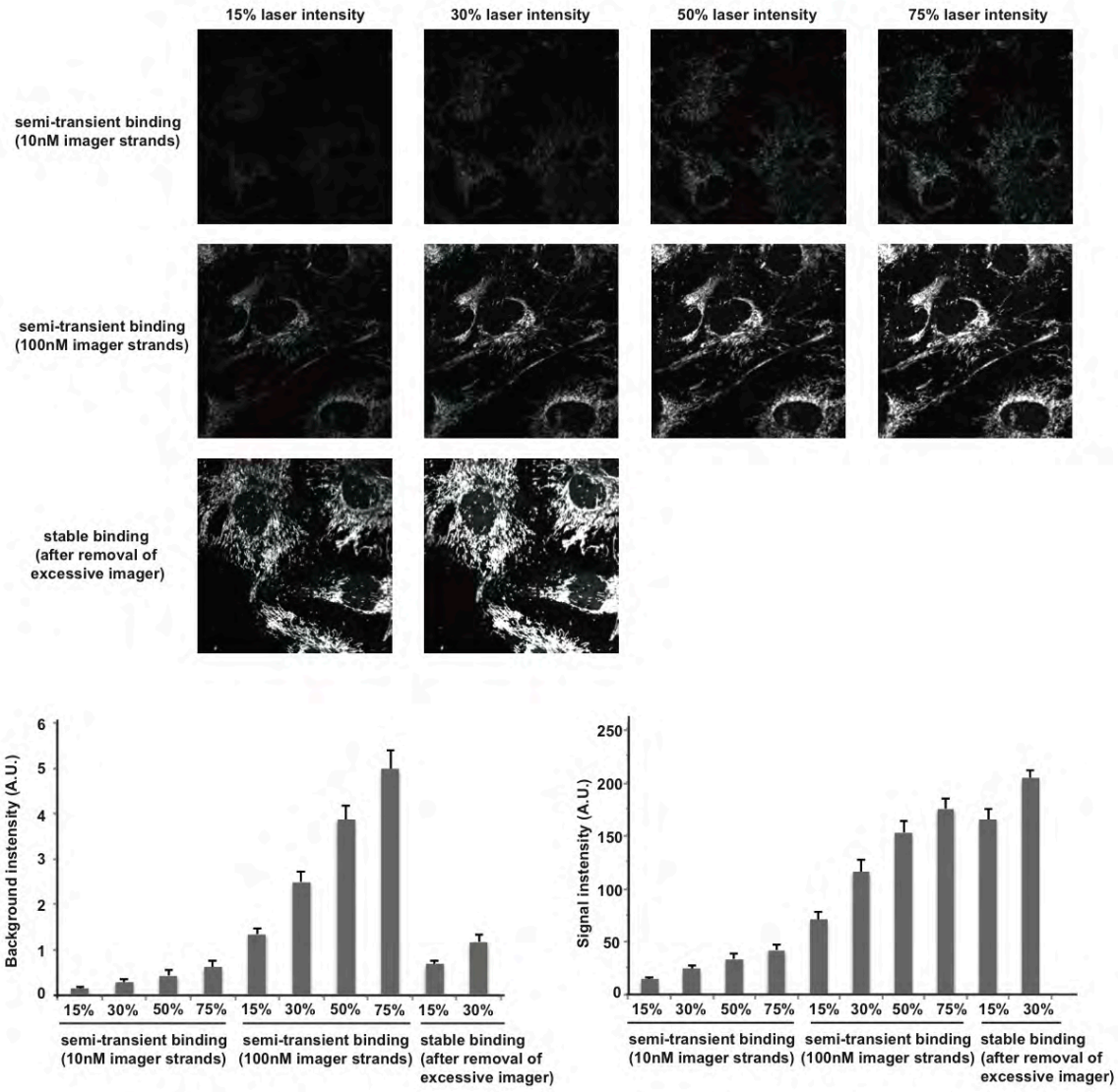

Figure S13. Comparison of imaging quality between semi-transient binding and stable binding schemes with mitochondria targets. BSC1 cells were fixed and labeled with antibodies targeting Tom20. Antibodies were conjugated with either 10-mer docking strands for semi-transient binding or 12-mer docking strands for stable binding. For semi-transient binding, we added 10 nM or 100 nM Alexa647-imager strands for imaging. For stable-binding, we incubated the cells with 1μM Alexa647-imager strands for 1 hour followed by 3 times buffer washing with 5 minutes for each to remove excessive imager strands. The laser intensity was set to 15%, 30%, 50% or 75% with gain 600. All 8-bit images were displayed with the same scale of 0-255. The error bar is SEM, n = 6.

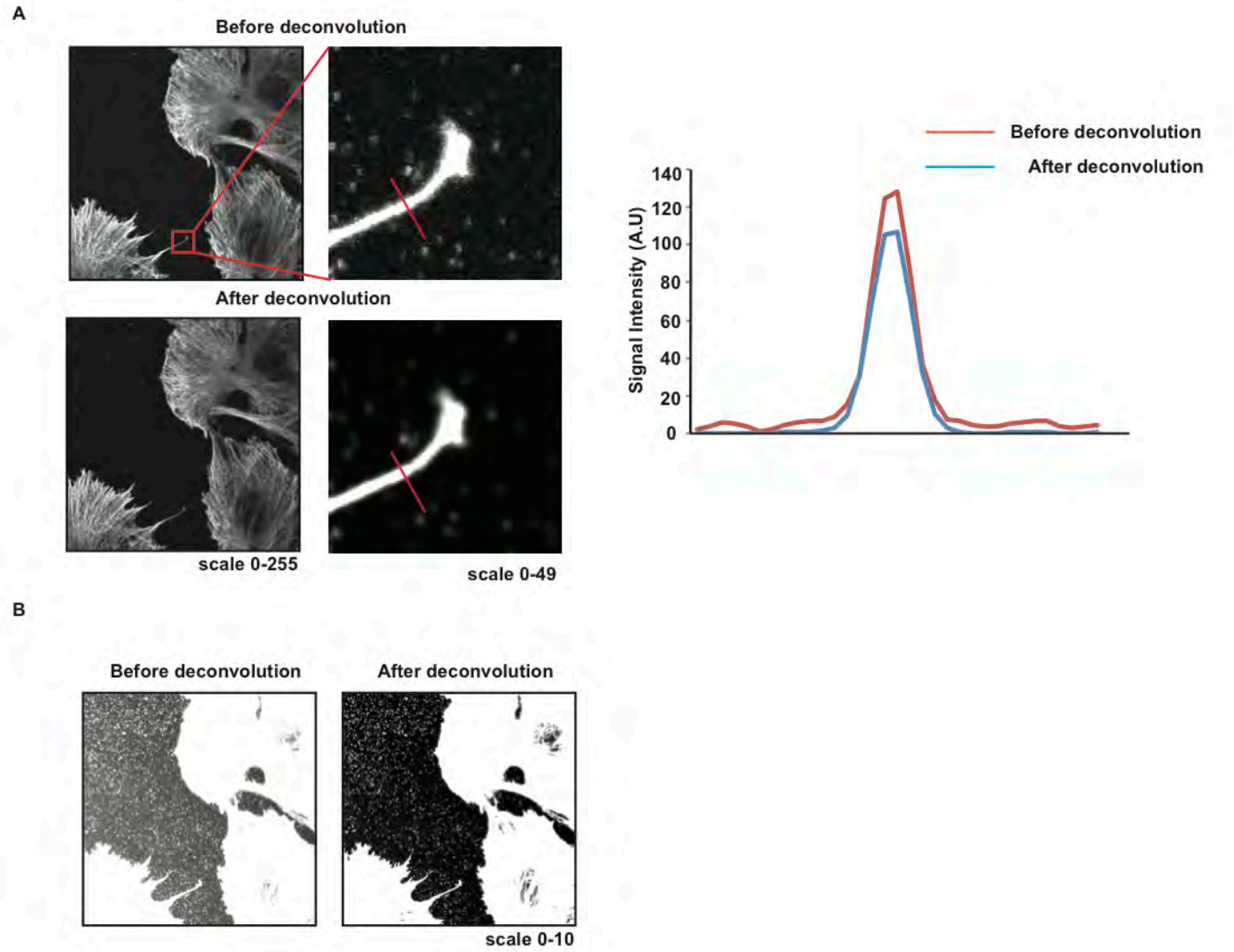

Figure S14. Image deconvolution on microtubule images in Figure S12. The deconvolution was performed using the Huygens software. A theoretical PSF and a deconvolution signal-to-noise parameter of 2 were used for deconvolution. **(A)** comparison of before and after deconvolution microtubule signals in semi-transient binding scheme (100nM imager strands at 75% laser intensity). One region in each image was selected for magnified view (marked in red square), and the signal profile of the indicated line was measured using FIJI. **(B)** The background of images was displayed by adjusting the contrast of the images.

Note: The results from Figures S12 and S13 were obtained under the same laser intensity illumination, stable binding scheme had higher signal, lower background and thus higher signal-to-background ratio compared with semi-transient binding. This is as expected because excessive imager strands in the buffer contribute to the background. In addition, in semi-transient binding scheme not all docking sites are occupied with imager strands, leading to decreased signals. Signal enhancement in semi-transient binding scheme can be achieved by further increasing the imager strands concentration (from 10 nM to 100 nM) to saturate the docking sites and by increasing laser intensity. Because of the continuous replenishment of imager strands in the semi-transient binding scheme, photobleaching is not a significant issue when laser intensity is high (also see **Figure S1**). Although semi-transient binding scheme had higher background, the background level was manageable and did not affect image visualization after adjusting the contrast. We think the low background attributed to the confocal imaging set up wherein the out-of-focus signal was blocked. This also applies to STED imaging. To further reduce background, we performed image deconvolution, an image processing method commonly used to improve image quality. It can be seen that after deconvolution, the signal of images became sharper and the background of image turned to ~0 in all images.

It should be noted that wide-field imaging could also be performed using semi-transient binding scheme if followed by image deconvolution. Indeed, the microscope used for the SIM experiment (**Figure 4**) is a wide-field microscope, and the SIM processing software automatically perform image deconvolution.

Comparison of DNA-Exchange-Imaging and other multiplexed protein imaging methods

Category	Subcategory	Method description	Reference	Comparison with DNA-Exchange-Imaging
Sequential antibody labeling	Antibody removal	Remove antibodies by denaturing using acidified glycine-SDS buffer or $KMnO_4$ or enzymatic digestion	5-8	1. The method requires repeated application of new antibodies after previous round of antibody removal or dye inactivation, and thus tends to be time consuming. Each round of staining typically takes 2 hours at room temperature and preferentially overnight at 4 °C for optimal labeling (e.g. Ref 9). 2. Harsh buffer treatment or laser treatment could potentially cause sample damage, e.g. cell loss. 3. Susceptible to photobleaching.
	Chemical bleaching of dyes	Dye inactivation using chemicals, e.g. 3% H_2O_2 and 20 mM NaOH	9, 10	
	Photobleaching of dyes	Dye inactivation with high power laser	11, 12	
Toehold mediated DNA probe replacement	-	Use eraser strand to remove dye-conjugated imager strand via toehold mediated branch migration	13, 14	1. The imager strand removal step requires explicit application of a complementary "eraser" strand that binds to the dye labeled imager strand. It thus involves more complex procedure and molecular constructs and tends to be more time consuming (e.g. in Ref.14, the imager removal took overnight compared with minutes in our DNA-Exchange-Imaging). 2. Susceptible to photobleaching as the imager strand is stably bound to the target before being explicitly removed using an eraser strand.
Spectral multiplexing	Quantum Dot	Use Q-Dots with more spectrally distinguishable colors than typical organic fluorophores	15	1. Limited multiplexing ability 2. Susceptible to chromatic aberration.
	Spectral imaging and linear unmixing	Integrate spectrum information with fluorescence imaging	16	1. Requires specialized instrument for spectrum detection 2. Uses computation algorithms to separate spectrally overlapping signals and is susceptible to artifacts generated by the unmixing algorithm.
	Spectrally resolved STORM	Integrate spectrum information with single-molecule based super-resolution STORM imaging	17	1. Uses single-molecule detection to separate spectrally overlapping signals, and is not directly applicable for diffraction-limited protein imaging. 2. Requires specialized instrument for spectrum detection.
Mass spectrometry imaging	Scanning mass cytometry (SMC) imaging	Laser ablation coupled with plasma time-of-flight mass spectrometry to detect isotope-labeled antibodies	18, 19	1. Destructive to samples. 2. Typically low resolution (1μm). 3. Require specialized instrument.
	Multiplexed ion beam imaging	Secondary ion mass spectrometry based ion beam scanning to detect isotope-labeled antibodies	19, 20	1. Repeated antibody staining (7 at a time) can be time-consuming. 2. Destructive to samples (although less than SMC). 3. Require specialized instrument.

Table S1. Overview of previous multiplexed protein target imaging methods and their comparison with DNA-Exchange-Imaging.

Description	Docking Strand Sequence	Imager Strand Sequence
P1	5’-TTTCTTCATTA-3’	5’-GTAATGAAGA-Dye
P2	5’-TTATCTACATA-3’	5’-TATGTAGATC-Dye
P3	5’-TTATGAATCTA-3’	5’-GTAGATTCAT-Dye
P4	5’-TTTCAATGTAT-3’	5’-CATACATTGA-Dye
P5	5’-TTAATTAGGAT-3’	5’-CATCCTAATT-Dye
P6	5’-TTAATTGAGTA-3’	5’-GTACTCAATT-Dye
P7	5’-TTTATATTGAC-3’	5’-CGTCAATATA-Dye
P8	5’-TTATGTTAATG-3’	5’-CCATTAACAT-Dye
P9 (10 nt)	5’-TTTCTTCATTAC-3’	5’-GTAATGAAGA-Dye
P10 (10 nt)	5’-TTGATCTACATA-3’	5’-TATGTAGATC-Dye
P11 (10 nt)	5’-TTATGAATCTAC-3’	5’-GTAGATTCAT-Dye
P12 (10 nt)	5’-TTAATTAGGATG-3’	5’-CATCCTAATT-Dye
P13 (10 nt)	5’-TTATGTTAATGG-3’	5’-CCATTAACAT-Dye
P14 (10 nt)	5’-TTAATTGAGTAC-3’	5’-GTACTCAATT-Dye
P15	5’-TTATAGTGATT-3’	5'-GAATCACTAT-Dye
P16 (10 nt)	5’-TTATACATCTAG-3’	5'-CTAGATGTAT-Dye
P17 (10 nt)	5’-TTTTAGGTAAAG-3’	5'-CTTTACCTAA-Dye
P18	5’-TTATAGTGATTC-3’	5'-GAATCACTAT -Dye

Table S2. DNA-Exchange-Imaging docking and imager strand sequences used in this study.

Target	Antibody	Species
AcetylTubulin	Invitrogen (32-2700)	Mouse
AlphaTubulin	ThermoFisher(MA1-80017)	Rat
Bassoon	Abcam (ab82958)	Mouse
Beta3Tubulin	ThermoFisher (MA1-19187)	Mouse
Chx10	ThermoFisher (PA1-12566)	Sheep
Cone arrestin	Millipore (AB15282)	Rabbit
Gephyrin	SynapticSystem (147108)	Human
GFAP	Invitrogen (13-0300)	Rat
GFAP	Encor (MCA-5C10-AP)	Mouse
GFP/YFP	Invitrogen (PA5-22688)	Rabbit
HER2	Dako #A0485	Rabbit
MAP2	SantaCruz (sc5359)	Goat
NeuN	Millipore (MAB377)	Mouse
pNFH	EnCor (CPCA-NF-H)	Chicken
SMA	Dako #M0851	Mouse
SV2	DSHB	Mouse
SynapsinI	Abcam (ab8)	Rabbit
SynapsinI/II	SynapticSystem (106004)	Guinea Pig
Synaptophysin	SynapticSystem (101004)	Guinea Pig
Tom20	SantaCruz (sc11415)	Rabbit
vGAT	SynapticSystem (131004)	Guinea Pig
Vimentin	Encor (CPCA-Vim)	Chicken
Vimentin	Biolegend (Poly29191)	Chicken

Table S3. Antibodies used in this study.

Target	DNA conjugates	Docking strand	Target	DNA Conjugates	Docking strand
SynapsinI	anti-rabbit secondary antibody	P11	GFAP	primary mouse antibody	P18
vGAT	anti-guinea pig secondary antibody	P12	MAP2	anti-goat secondary antibody	P13
pNFH	anti-chicken secondary antibody	P14	AlphaTubulin	anti-rat secondary antibody	P10
AcetylTubulin	primary mouse antibody	P15	Gephyrin	anti-human secondary antibody	Alexa488

Table S4. Antibodies and conjugated DNA docking strands for multiplexed diffraction-limited imaging in primary neuron culture.

Target	DNA conjugates	Docking strand	Target	DNA conjugates	Docking strand
SV2	primary mouse antibody	P16	GFAP	anti-rat secondary antibody	P10
Cone arrestin	anti-rabbit secondary antibody	P11	Chx10	anti-sheep secondary antibody	P13
Vimentin	anti-chicken secondary antibody	P14	Synapsin	anti-guinea pig secondary antibody	P12

Table S5. Antibodies and conjugated DNA docking strands for multiplexed diffraction-limited imaging in retina sections.

Target	DNA conjugates	Docking strand	Target	DNA conjugates	Docking strand
GFAP	anti-rat secondary antibody	P10	YFP	Anti-rabbit secondary antibody	P11
pNFH	anti-chicken secondary antibody	P14	NeuN	anti-mouse secondary antibody	P9

Table S6. Antibodies and conjugated DNA docking strands for multiplexed diffraction-limited imaging in mouse brain sections.

Target	DNA conjugates	Docking strand	Target	DNA conjugates	Docking strand
HER2	anti-rabbit secondary antibody	P11	SMA	anti-mouse secondary antibody	P9

Table S7. Antibodies and conjugated DNA docking strands for multiplexed diffraction-limited imaging in breast tumor sections.

Target	DNA conjugates	Docking strand	Target	DNA conjugates	Docking strand
alphaTubulin	anti-rat secondary antibody	P10	betaTubulin	anti-mouse secondary antibody	P9
Tom20	anti-rabbit secondary antibody	P11	Vimentin	anti-chicken secondary antibody	P17

Table S8. Antibodies and conjugated DNA docking strands for multiplexed SIM imaging.

Target	DNA conjugates	Docking strand	Target	Dna conjugates	Docking strand
SynapsinI	anti-rabbit secondary antibody	P11	Bassoon	anti-mouse secondary antibody	P9
pNFH	anti-chicken secondary antibody	P14	GFAP	anti-rat secondary antibody	P10

Table S9. Antibodies and conjugated DNA docking strands for multiplexed STED imaging.

Target	DNA conjugates	Docking strand	Target	DNA conjugates	Docking strand
SynapsinI	anti-rabbit secondary antibody	P3	Bassoon	anti-mouse secondary antibody	P1
vGAT	anti-guinea pig secondary antibody	P5	Vimentin	anti-chicken Secondary antibody	P6
Tom20	anti-rabbit secondary antibody	P4	AlphaTubulin	anti-rat secondary antibody	P2
GFAP	primary mouse antibody	P18	AcetylTubulin	Primary mouse antibody	P7

Table S10. Antibodies and conjugated DNA docking strands for multiplexed super-resolution PAINT imaging.

WF_FWHM	SIM_FWHM	Ratio
358.9	178.5	2.0
346.6	179.5	1.9
303.6	188.0	1.6
301.4	149.6	2.0
392.8	186.6	2.1
449.3	224.6	2.0
251.9	139.7	1.8
348.2	194.9	1.8
363.0	169.6	2.1
333.6	149.6	2.2
404.2	175.7	2.3
316.8	177.9	1.8
436.6	205.7	2.1
382.6	171.2	2.2
510.6	226.2	2.3
426.0	222.5	1.9
305.1	155.8	2.0
360.0	200.2	1.8
299.0	157.5	1.9
332.4	139.6	2.4

Table S11. Full width at half maximum data of microtubule cross-sections obtained from SIM alphaTubulin imaging.

Binding scheme	Transient	Semi-transient	Stable
Pros	1. Fast blinking frequency that allows DNA-PAINT imaging 2. Easy removal of signal from the previous cycle 3. Resistant to photobleaching 4. Faster imaging as no need to remove excessive imager strands	1. Longer binding duration on docking sites enables confocal and other platform imaging 2. Easy removal of signal from the previous cycle 3. Resistant to photobleaching 4. Faster imaging as no need to remove excessive imager strands	1. Superior signal-to-background ratio 2. Suitable for widefield and STORM imaging
Cons	1. Only suitable for DNA-PAINT imaging 2. Requires high signal-to-background ratio microscopy (e.g. TIRF, light sheet, spinning disc confocal) for imaging	1. Not suitable for STORM imaging. Widefield imaging requires post-imaging deconvolution processing. 2. Lower signal-to-background compared with stable binding; requires experimental adjustment of imager strand concentration and laser intensity to get optimal imaging setting	1. Requires long incubation time and additional wash to remove excessive imager strands prior to imaging. 2. Requires harsher washing condition (e.g. 30% formamide for 12mer) to remove signal from the previous cycle. 3. Sensitive to photobleaching
Application	DNA-PAINT	Confocal, SIM, STED, Expansion microscopy	Widefield, Confocal, SIM, STED, STORM, Expansion microscopy

Table S12. Comparison between transient, semi-transient and stable DNA binding schemes.

Movie caption:

3D views of multi-targets in fixed mouse hippocampal neuron cultures. A movie was created using Imaris for 3D slicing views of the targets shown in Figure 2. Mouse hippocampal neurons were fixed using PFA and stained to target SynapsinI, vGAT, MAP2, pNFH, AlphaTubulin, AcetylTubulin, GFAP, and DAPI.

References

(1) Behbod, F.; Kittrell, F. S.; LaMarca, H.; Edwards, D.; Kerbawy, S.; Heestand, J. C.; Young, E.; Mukhopadhyay, P.; Yeh, H. W.; Allred, D. C.; Hu, M.; Polyak, K.; Rosen, J. M.; Medina, D. *Breast Cancer Res* **2009,** 11, (5), R66.

(2) Jungmann, R.; Avendano, M. S.; Woehrstein, J. B.; Dai, M.; Shih, W. M.; Yin, P. *Nat Methods* **2014,** 11, (3), 313-8.

(3) Guizar-Sicairos, M.; Thurman, S. T.; Fienup, J. R. *Opt Lett* **2008,** 33, (2), 156-8.

(4) Agasti, S. S.; Wang, Y.; Schueder, F.; Sukumar, A.; Jungmann, R.; Yin, P. *Chem Sci* **2017,** 8, (4), 3080-3091.

(5) Gerdes, M. J.; Sevinsky, C. J.; Sood, A.; Adak, S.; Bello, M. O.; Bordwell, A.; Can, A.; Corwin, A.; Dinn, S.; Filkins, R. J.; Hollman, D.; Kamath, V.; Kaanumalle, S.; Kenny, K.; Larsen, M.; Lazare, M.; Li, Q.; Lowes, C.; McCulloch, C. C.; McDonough, E.; Montalto, M. C.; Pang, Z.; Rittscher, J.; Santamaria-Pang, A.; Sarachan, B. D.; Seel, M. L.; Seppo, A.; Shaikh, K.; Sui, Y.; Zhang, J.; Ginty, F. *Proc Natl Acad Sci U S A* **2013,** 110, (29), 11982-7.

(6) Glass, G.; Papin, J. A.; Mandell, J. W. *J Histochem Cytochem* **2009,** 57, (10), 899-905.

(7) Lin, J. R.; Fallahi-Sichani, M.; Sorger, P. K. *Nat Commun* **2015,** 6, 8390.

(8) Pirici, D.; Mogoanta, L.; Kumar-Singh, S.; Pirici, I.; Margaritescu, C.; Simionescu, C.; Stanescu, R. *J Histochem Cytochem* **2009,** 57, (6), 567-75.

(9) Micheva, K. D.; Smith, S. J. *Neuron* **2007,** 55, (1), 25-36.

(10) Tam, J.; Cordier, G. A.; Borbely, J. S.; Sandoval Alvarez, A.; Lakadamyali, M. *PLoS One* **2014,** 9, (7), e101772.

(11) Friedenberger, M.; Bode, M.; Krusche, A.; Schubert, W. *Nat Protoc* **2007,** 2, (9), 2285-94.

(12) Schubert, W.; Bonnekoh, B.; Pommer, A. J.; Philipsen, L.; Bockelmann, R.; Malykh, Y.; Gollnick, H.; Friedenberger, M.; Bode, M.; Dress, A. W. *Nat Biotechnol* **2006,** 24, (10), 1270-8.

(13) Duose, D. Y.; Schweller, R. M.; Hittelman, W. N.; Diehl, M. R. *Bioconjug Chem* **2010,** 21, (12), 2327-31.

(14) Schweller, R. M.; Zimak, J.; Duose, D. Y.; Qutub, A. A.; Hittelman, W. N.; Diehl, M. R. *Angew Chem Int Ed Engl* **2012,** 51, (37), 9292-6.

(15) Zrazhevskiy, P.; Gao, X. *Nat Commun* **2013,** 4, 1619.

(16) Zimmermann, T.; Marrison, J.; Hogg, K.; O'Toole, P. *Methods Mol Biol* **2014,** 1075, 129-48.

(17) Zhang, Z.; Kenny, S. J.; Hauser, M.; Li, W.; Xu, K. *Nat Methods* **2015,** 12, (10), 935-8.

(18) Giesen, C.; Wang, H. A.; Schapiro, D.; Zivanovic, N.; Jacobs, A.; Hattendorf, B.; Schuffler, P. J.; Grolimund, D.; Buhmann, J. M.; Brandt, S.; Varga, Z.; Wild, P. J.; Gunther, D.; Bodenmiller, B. *Nat Methods* **2014,** 11, (4), 417-22.

(19) Levenson, R. M.; Borowsky, A. D.; Angelo, M. *Lab Invest* **2015,** 95, (4), 397-405.

(20) Angelo, M.; Bendall, S. C.; Finck, R.; Hale, M. B.; Hitzman, C.; Borowsky, A. D.; Levenson, R. M.; Lowe, J. B.; Liu, S. D.; Zhao, S.; Natkunam, Y.; Nolan, G. P. *Nat Med* **2014,** 20, (4), 436-42.